JOURNAL OF GEOPHYSICAL RESEARCH, VOL. 104, NO. E6, PAGES 14,065–14,089, JUNE 25, 1999

Mars mapping with delay-Doppler radar

John K. Harmon,[1] Raymond E. Arvidson,[2] Edward A. Guinness,[2]
Bruce A. Campbell,[3] and Martin A. Slade[4]

Abstract. Mars radar imaging results from Arecibo 12.6-cm observations are presented. The images were derived from delay-Doppler mapping using a coded-long-pulse technique to mitigate the effects of echo overspreading. Images of the depolarized echo are used to identify regions of high decimeter-scale roughness. Some of the strongest echo features are located on the major shield volcanoes or on relatively young off-shield flows such as the Olympus and Pavonis lava aprons. The shields themselves have highly irregular radar signatures suggesting complex volcanic histories. Some Mars radar features have twice the depolarized brightness of the roughest terrestrial lava flows, apparently due to higher levels of multiple scattering from surfaces of spectacular roughness or from volume scattering. Low-brightness (smooth) areas are associated with older surfaces such as fractured and highland terra, as well as with terrain interpreted to be debris lobes, ash flows, and aureoles; in particular, a close connection was found between the 12.6-cm counterpart of the "Stealth" feature and the Medusae Fossae Formation (postulated to be deep ignimbrite deposits). Marte Vallis is anomalous in being the only outflow channel showing strongly enhanced echoes, which supports the idea that this channel and the Elysium Basin that it drained are filled with lava flows. A weak radar feature was found for the south polar residual ice cap. Comparisons with Goldstone 3.5-cm data show that the south polar enhancement is much weaker at 12.6 cm than at 3.5 cm, indicating that the southern ice cap becomes optically thin at the longer wavelength. A north polar enhancement has also been found, which is comparable in strength to the 12.6-cm south polar feature.

1. Introduction

The surface of Mars shows extreme diversity in its radar scattering properties [*Simpson et al.*, 1992]. This diversity is seen in both the quasi-specular and diffuse components of the echo. (The quasi-specular echo, which is completely polarized, is associated with mirror-like reflections from superwavelength-scale surface undulations; the diffuse echo, which is partially depolarized, is associated with wide-angle scattering from wavelength-scale roughness.) Early continuous wave (CW) radar studies of the polarized echo revealed strong spatial variations in quasi-specular reflectivity, indicative of variations in effective surface dielectric constant [*Goldstein*, 1965; see also *Jakosky and Muhleman*, 1981]. Numerous observations in the 1970s (both CW and ranging-type) showed that there are also large spatial variations in quasi-specular roughness [*Simpson et al.*, 1978a, b]. In the early 1980s, dual-polarization CW measurements of the full Mars echo showed evidence for strongly enhanced levels of diffuse radar backscatter from the major volcanic provinces [*Harmon et al.*, 1982; *Harmon and Ostro*, 1985]. These diffuse enhancements show up particularly well in the depolarized component of the diffuse echo because (1) the depolarized echo is free from quasi-specular glare and (2) the degree of depolarization is higher in the enhancements. The natural conclusion was drawn that the depolarized enhancements represent backscatter from lava flows which are extremely rough on wavelength (decimeter) scales [*Harmon et al.*, 1982; *Harmon and Ostro*, 1985; *Thompson and Moore*, 1989]. However, these results were based solely on CW Doppler spectra, from which only crude spatial mapping information can be extracted. At that time it was clear that further progress on the large-scale radar mapping of Mars' diffuse echo would require more sophisticated radar techniques.

The most common radar-mapping technique is the so-called "delay-Doppler" method. This approach has been used with great success in Earth-based radar mapping of Venus [*Campbell and Burns*, 1980]. The stan-

[1]Arecibo Observatory, National Astronomy and Ionosphere Center, Arecibo, Puerto Rico.
[2]Department of Earth and Planetary Sciences, Washington University, St. Louis, Missouri.
[3]National Air and Space Museum, Washington, DC.
[4]Jet Propulsion Laboratory, California Institute of Technology, Pasadena, California.

Paper number 1998JE900042..
0148-0227/99/1998JE900042$09.00

dard type of delay-Doppler mapping involves coherent spectral analysis using inter-pulse or inter-code sampling. This requires that the target echo be "underspread," i.e., that the time-bandwidth product of the echo not exceed unity. Mars, unlike Venus, is grossly overspread and therefore cannot be mapped with this technique, although some topography and scattering information can be extracted from the leading edge of the planet's delay-Doppler echo [*Downs et al.*, 1975, 1982]. One can also do a crude delay-Doppler mapping of Mars using intrapulse coherent analysis [*Dyce et al.*, 1967], but the achievable resolution is too coarse to be of much use.

The first true radar images of Mars were obtained in 1988 from X-band (3.5-cm wavelength) bistatic observations involving transmission at Goldstone and reception at the Very Large Array (VLA) [*Muhleman et al.*, 1991; *Butler*, 1994; *Muhleman et al.*, 1995]. The images were formed directly using the VLA synthesized beam rather than by delay-Doppler mapping. Besides locating the sources of some of the major volcanic backscatter enhancements, the Goldstone/VLA images produced two major surprises: the detection of a very strong echo from the south polar ice cap (reminiscent of the anomalous echoes from the icy Galilean satellites) and the discovery of a large radar-dark area in southern Amazonis (dubbed "Stealth").

A considerable effort was made in the 1980s to perfect techniques for dealing with the overspreading problem in ionospheric radar observations. It was realized that one technique in particular, the coded-long-pulse (CLP) method, could be adapted to the delay-Doppler mapping of overspread planets. We therefore undertook a series of Mars radar observations using this technique at Arecibo, the objective being to image the planet at a different wavelength and with a finer resolution than was possible with the VLA. (The VLA image resolution was limited by the 170-km diameter of the synthesized beam at the distance of Mars). The first CLP observations of Mars were made with the Arecibo S-band (12.6-cm wavelength) radar during the 1990 opposition. Shortly thereafter, the same technique was used to image Mercury [*Harmon and Slade*, 1992; *Harmon et al.*, 1994b; *Harmon*, 1997a] and to range Ganymede and Callisto [*Harmon et al.*, 1994a]. A preliminary report of the 1990 Mars results [*Harmon et al.*, 1992b] concentrated on describing the unusual radar features in Elysium. Since then, more observations have been made (during the 1992–1993 opposition), and work has been done on improving the quality of all the 1990–1993 images by summing multiple observing runs. Of that work, those results dealing specifically with the Chryse channel region and spacecraft lander sites were recently reported by *Harmon* [1997b] and will not be discussed further in this paper. We will also not discuss the heavily cratered highlands dominating the Southern Hemisphere, a region that appears as relatively weak and featureless in our radar images. Although there is some evidence for some slightly enhanced features in the south (e.g., from the Hellas and Argyre basin rims), the low echo strength and sparser data coverage make for relatively poor images and less reliable N/S-ambiguity detection over this region. Instead, we will limit ourselves here to making a comprehensive presentation and geologic description of the 1990–1993 CLP results for Mars' major volcanic provinces and polar ice caps.

2. Data and Analysis

2.1. Observations

2.1.1. Observing epochs. Limited system sensitivity and the inverse-fourth-power distance dependence for the echo strength restrict radar imaging of Mars to a few months around opposition. Our first observing campaign was conducted during the 1990 opposition. The 1990 images shown in this paper were derived from several nights of observation between November 5 and December 16, 1990. During this period the sub-Earth latitude changed from 4.8°S to 12.1°S. Our second campaign was conducted during the 1992–1993 opposition. The data from that campaign that are used in this paper were obtained on several nights between December 7, 1992 and January 28, 1993, during which time the sub-Earth latitude changed from 12.2°N to 4.3°N.

2.1.2. Observing setup. The observations were made with the S-band (2380 MHz, 12.6-cm wavelength) radar on the 1000-foot Arecibo telescope. The transmitted power was typically about 400 kW. The transmitted wave was biphase coded with baud lengths of either 100 (1990) or 70 μs (1992–1993); it was this baud length that determined the delay resolution of the data. A circularly polarized wave was transmitted, and both the same-sense ("SC" or "depolarized") and opposite-sense ("OC" or "polarized") circular polarizations were received. The transmitted code was a $2^{39} - 1$ maximal-length shift register sequence, which, contrary to standard coding practice, did not repeat during the course of an observing run. Since the code generator was a noninitializable (free running) device, the replica code for decoding was determined by sampling the transmitter leakage signal during the transmit cycle.

Up to six observing "runs" were made on any given night. A run consisted of a transmit period and a receive period, each with a duration of one round-trip light travel time. The transmitter was shut off for the last 2 min of the transmit period, providing 2 min of echo-free noise at the end of the receive period for calibration purposes. The receiver output was quadrature mixed to base band and passed through a filter matched to the baud. The matched-filtered signals were then complex sampled once per baud and stored for further processing.

2.2. Delay-Doppler Analysis

2.2.1. Decoding and spectral analysis. In the standard delay-Doppler analysis the decoding is done by cross correlating the received signal with the replica

code. The decoding yields one sample of the complex voltage for each lag (or delay bin) for each code repetition cycle. Decoding successive code cycles produces a complex voltage time series for each delay. Taking the Fourier transform and squared modulus (i.e., the power spectrum) of these time series gives a single statistical realization (or "look") of the echo power distribution in delay-Doppler space. Successive realizations of this "delay-Doppler array" are then summed incoherently to reduce the rms noise fluctuation level.

The scheme just described works well if the time-bandwidth product $B\tau$ of the planet's delay depth τ and rotational Doppler bandwidth B is less than unity. In this case one can set the code repetition period to some value $\geq \tau$ and still satisfy the Nyquist condition for critically sampling the Doppler spectrum. If the target is "overspread" ($B\tau > 1$), then one cannot avoid some aliasing of the delay-Doppler array in either delay or Doppler. However, in some cases one can still make useful estimates of the full delay-Doppler array if, instead of cross correlating (i.e., summing lagged products of) the data and replica code, one Fourier transforms the lagged products directly without the correlation summing [*Sulzer*, 1986, 1989; *Hagfors and Kofman*, 1991]. In this case the sampling rate for the spectral analysis is the raw data sampling rate (typically once or twice per baud) rather than the code repetition rate, so the Nyquist frequency can be much higher. The price paid for not cross correlating is the addition of a clutter component to the spectrum for each delay. This clutter comes from the product of the replica code with the echo signals from all of the other ("wrong") delays. However, if a nonrepeating code is used instead of the usual repeating code, then the clutter contribution reduces to an additive noise component that only lowers the signal-to-noise ratio. This is the essence of the "coded-long-pulse" method used in incoherent scatter radar measurements of the ionosphere [*Sulzer*, 1986, 1989]. We will adopt the name coded long pulse for the equivalent method used in this paper, even though our S-band radar employs continuous transmission rather than the pulsed transmission commonly used by the lower-frequency ionospheric radars.

We adopted *Sulzer*'s [1986] method for the delay-Doppler analysis of our received signal. First, the various lagged-product time series were formed by multiplying the complex receive signal by the transmitted code. Then the lagged-product time series (for a given delay bin) was partitioned into n length transform buffers, where n=512 for the 1990 data and n=1024 for the 1992–1993 data. The power spectrum was computed for each buffer, and the spectra from successive buffers were summed over the integration period. This process was applied to each delay bin (lag), giving a raw delay-Doppler array with 260 delays and 512 frequencies (for 1990) or 360 delays and 1024 frequencies (for 1992–1993). The Nyquist frequencies of the spectra were ±5 kHz (1990) or ±7.14 kHz (1992–1993). The delay and Doppler resolutions were 100 μs and 19.53 Hz (for 1990) or 70 μs and 13.95 Hz (for 1992–1993). The echo receive period (the round-trip time minus the 2-min noise period) for each observing run was divided into two integration periods of about 4-min duration each.

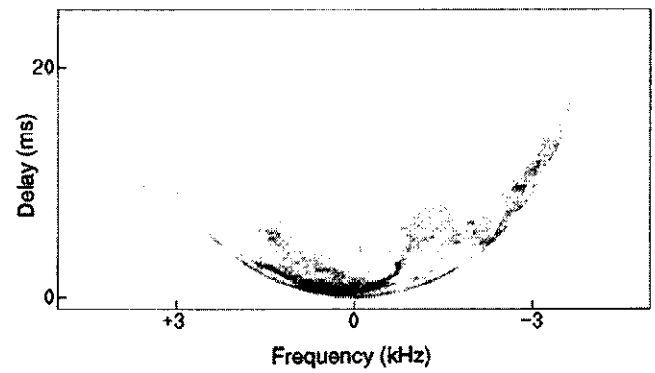

Figure 1. Delay-Doppler array of Mars echo power from one run on December 1, 1990. The mean receive time is 0334 UT and the integration time is 6 min, 40 s. Darker shading corresponds to higher echo power. The dominant echo feature behind the leading edge is from the Elysium Basin and Marte Vallis.

The next stage of the analysis involved subtraction of a noise baseline level from each lag of the delay-Doppler array. Since the signal was sampled once per baud, the total noise spectrum (the sum of true system noise and clutter) is flat, so that the noise was easily subtracted by estimating the baseline level using the frequencies outside the echo band. An example of a delay-Doppler array with noise subtracted is shown in Figure 1. The percentage contribution of the clutter to the total noise level was found to be precisely as expected (see next section), varying between 15% and 71%, depending on the epoch. However, in addition to the random component, the clutter was also found to contain some nonrandom ripples associated with spurious zero-mean oscillations in 8 out of the first 260 delay bins of the delay-Doppler ambiguity function. Test simulations showed that this nonrandomness is caused by a combination of small system phase errors and the peculiarities of the two-feedback-tap implementation of the $2^{39} - 1$ code. This ripple problem had a negligible effect on the SC images shown this paper but is clearly noticeable in the delay-Doppler arrays of the OC echo owing to leakage of the strong specular echo from the subradar point. Simulations showed that this problem can be avoided in the future by using shift-register codes with four instead of two feedback taps.

2.2.2. Calibration. After subtraction of the noise baseline, the delay-Doppler array for each integration period was converted into an array of radar cross-section estimates. First, the array was normalized to true echo power. This was done by multiplying the array values by $kT\Delta f/N$, where k is Boltzmann's constant, T is the system temperature, Δf is the Doppler resolution, and N is that portion of the baseline level due to system noise and not clutter. We estimated N in two different

ways, comparing the results for consistency. The first way was to determine N from the level of the spectrum of the 2-min echo-free (hence clutter free) period at the end of the run. The second method involved using the delay bins in front of the echo to estimate a level that included system noise plus a clutter contribution from the entire echo, then subtracting a clutter level estimated by summing the echo power from all delays and spreading that power evenly over the full spectral bandwidth. The N estimates from the two methods gave excellent agreement (typically better then 5%). The final step in the reduction was to convert the delay-Doppler array from power values to radar cross-section values. This was done by dividing by the radar-equation factor $PG^2\lambda^2/(64\pi^3R^4)$, where P is transmitter power, G is antenna gain, λ is radar wavelength, and R is the Mars distance.

The calibration was checked by comparing depolarized albedos $\hat{\sigma}_{sc}$ (the full-disk SC cross section divided by the projected area πR^2 of the planet) estimated from our CLP delay-Doppler arrays with values estimated from older CW Doppler spectra. This $\hat{\sigma}_{sc}$ is a useful parameter for consistency checks of this kind because of its relatively slow variation with sub-Earth position. Figure 2 shows a comparison of our CLP albedos with CW albedos obtained at Arecibo from 1980–1990; here the CLP values have been multiplied by a 3/2 factor to correct for the fact that the integral under the triangle-squared delay response function (or "ambiguity function") is 2/3. This figure shows good agreement between our new CLP results and the older, more easily calibrated CW results. These Arecibo CW values are themselves in good agreement with depolarized albedos obtained with the Goldstone radar at the same wavelength [*Thompson and Moore*, 1989; *Moore and Thompson*, 1991].

2.3. Mapping

2.3.1. Mapping algorithm and images. The mapping algorithm converts the delay-Doppler arrays (which give radar cross section in delay-Doppler space) into images of SC specific cross section σ^o_{sc} in planetary (longitude-latitude) coordinates. The images are 466×708 raster arrays with each pixel measuring about 0.1° on a side. A raw image (or "snapshot") was formed for each half-run ($\approx$ 4 min) integration period. The snapshots from between three and five runs (6–10 integration periods) were then averaged to increase the signal-to-noise ratio. This was a weighted average that included a $\cos^{1.5}\theta$ factor in the weighting to account for the expected falloff in the scattering law $\sigma^o_{sc}(\theta)$ with increasing incidence angle θ. The averaged image was then smoothed over boxes of 7×7 pixels to give the final image. The 7×7 smoothing corresponds to an effective resolution cell measuring about 0.66° on a side. For comparison, the intrinsic longitude resolution in a snapshot (determined mainly by the longitude smearing from planet rotation during the 4-min integration period) is about 1.0°, or about 3 times the width of a Doppler strip. The intrinsic latitude resolution, set by the baud length, is about 0.25° at the poles, becoming coarser by a factor of $1/\sin(\text{lat})$ owing to geometrical projection as one approaches the equator. The delay (hence latitude) resolution cell also stretches somewhat with increasing Doppler shift owing to increasing cutoff from the matched filter. This effect, which comes into play when the target bandwidth is a substantial fraction of the sampling bandwidth, can be mitigated in future observations by combining a wider (unmatched) filter with a higher (more than once per baud) sampling rate.

The reflectivity image is normalized to give specific cross section σ^o_{sc}, which is defined as the radar cross

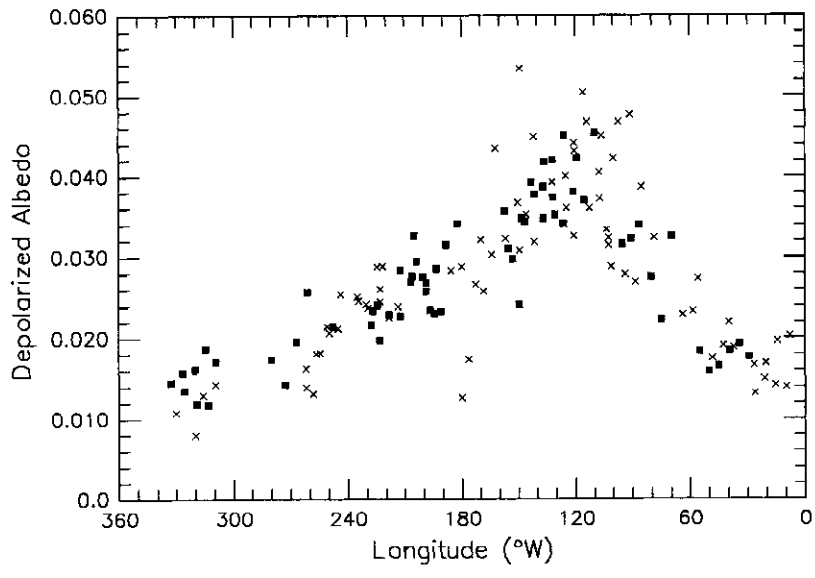

Figure 2. Full-disk depolarized albedo $\hat{\sigma}_{sc}$ versus sub-Earth longitude for the Arecibo 1990–1993 coded-long-pulse (CLP) delay-Doppler data (squares) and Arecibo 1980–1990 continuous wave (CW) data (crosses).

section per unit surface (not projected) area. For the normalizing area we use the mapped area of the delay-Doppler cell multiplied by the 3/2 factor mentioned in the last section. Although each delay-Doppler cell includes the echoes from conjugate points north and south of the Doppler equator, we have normalized by the surface area of one rather than both points. This gives a better estimate of the σ^o_{sc} for any strong feature whose contribution overwhelms that from its conjugate point. The alternative would have been to normalize by the area of both conjugate points, which would have resulted in a large underestimation of the absolute strength of those very bright features in which we are most interested. The absolute calibration of the mapping algorithm was tested by comparing the total cross sections computed by summing over whole blocks of range gates in the delay-Doppler arrays with sums over the corresponding delay annuli in the final planet maps. The comparisons showed good agreement.

2.3.2. Mapping ambiguity. The aforementioned N/S mapping ambiguity can be a major complication in the interpretation of delay-Doppler radar images. This ambiguity can be resolved to some extent by observing the same part of the planet at different sub-Earth latitudes and comparing the images. In principle, one can construct an unambiguous image by combining snapshot images using a rigorous analytic algorithm; in practice, such methods are very complex and often produce degraded images because of their sensitivity to noise, calibration error, and scattering-law assumptions. For this paper we have simply inspected pairs of images taken at different sub-Earth latitudes in order to distinguish real features from those which are associated with (or significantly corrupted by) foldover from the conjugate hemisphere. Our data set was well suited for these comparisons because of the large range of sub-Earth latitudes covered over the two oppositions. Any prominent radar feature that is mentioned in the next section has been checked for fold-over by such visual inspection. Those features in our images (Figures 3, 4, and 7) that were found to be fold-over artifacts or to have significant fold-over confusion are identified by crosshatching in the accompanying sketch maps.

3. Results by Region

This section is devoted to a (largely qualitative) description of the imaging results on a regional basis. Here our implicit working assumption will be that areas giving strong radar backscatter correspond to surfaces with relatively high decimeter-scale roughness. A more quantitative discussion of the implications of the strong echoes from the volcanic regions is deferred to section 4. The polar ice caps echoes, which are special cases, will be treated separately in section 5.

In this discussion we will make reference to Mars geologic units as defined in the geologic maps in the U.S. Geological Survey I-1802 series [*Scott and Tanaka*, 1986;

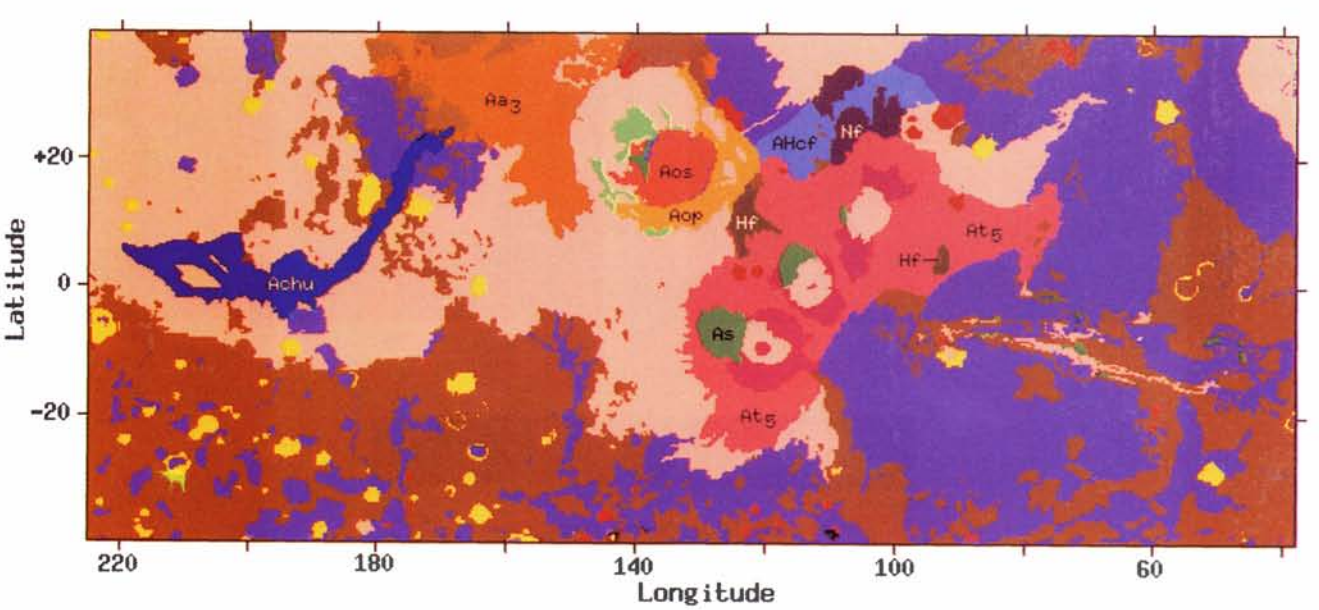

Plate 1. Simplified geologic map of Mars, adapted from the maps of *Scott and Tanaka* [1986] and *Greeley and Guest* [1987]. Letter labels correspond to geologic terrain units mentioned in the text: Aop, Olympus Mons Formation plains member; Aos, Olympus Mons Formation shield member; At_5, Tharsis Montes Formation member 5; Achu, channel and flood plain (Elysium Basin and Marte Vallis); Aa_3, Arcadia Formation member 3; AHcf, Ceraunius Fossae Formation; Nf, older fractured material (Ceraunius Fossae); Hf, younger fractured material (Ulysses Fossae and Fortuna Fossae); and As, slide material (Tharsis volcano debris). All these units are of Amazonian age, except for unit Hf (Hesperian) and unit Nf (Noachian). Other Hesperian units are denoted by the purple shade (mostly ridged plains or Syria Planum Formation). Other Noachian units are denoted by the brown shade (mostly plateau sequence of the cratered highlands).

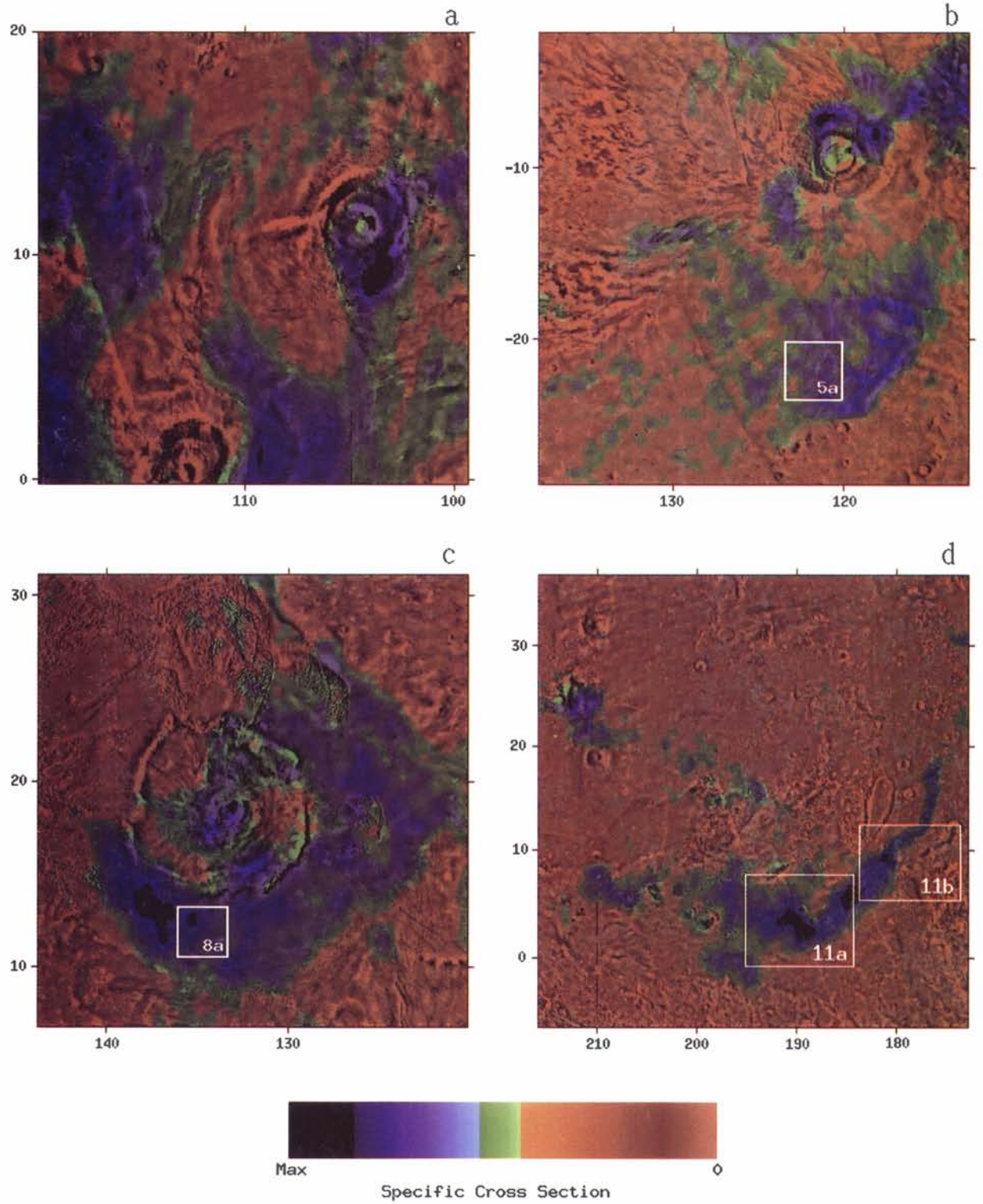

Plate 2. Color-coded radar images of depolarized radar cross section σ^o_{sc} for selected regions superimposed on Viking visible image mosaics. (a) Northern Tharsis, including the shields of Pavonis Mons (bottom left) and Ascreaus Mons (top right). (b) Southern Tharsis and Daedalia Planum, including the Arsia Mons shield (top right); the box gives the location of the Viking image of east Daedalia shown in Figure 5a. (c) Olympus Mons region with the Olympus Mons shield visible just left of center; the box gives the location of the Viking image of the Olympus lava apron shown in Figure 8a. (d) Elysium region, including the Elysium shields (top left); the boxes give the locations of the Viking images of Elysium Basin and Marte Vallis shown in Figures 11a and 11b. The color bar has a linear scale with max = 0.211, 0.363, 0.254, and 0.209 for Plates 2a, 2b, 2c, and 2d, respectively. The zero point for Plates 2b and 2d is as shown on the color bar; for Plates 2a and 2c the zero points are at 9% max and 13% max, respectively.

Greeley and Guest, 1987]. A simplified composite of these geologic maps is shown in Plate 1. The radar-mapping results are presented in several regional-scale images and their accompanying sketch maps (Figures 3, 4, 7, and 10) as well as in Plate 2 (which shows color-coded images of selected areas overlayed on Viking image mosaics).

The images (Figures 3, 4, 7, and 10) are represented on a gray scale, with darker shades corresponding to higher specific cross section σ^o_{sc}. The quoted cross sections are given both as regular numbers as well as on the logarithmic decibel (dB) scale used commonly in Earth remote sensing, where $\sigma^o_{sc}(\mathrm{dB}) = 10\ \log_{10} \sigma^o_{sc}$. The effective incidence angle varies across any given image, so that the relative intrinsic strength of any two features on a given image cannot necessarily be determined by direct comparison of shade. Some information on the ranges of incidence angles is given in the figure captions, and the incidence angles θ for some of the more prominent features are given in the text.

In this section and the rest of the paper we will use the terms "bright" (or "radar bright") and "dark" (or "radar dark") as a shorthand to describe regions with relatively high radar cross section (strong echo) or low radar cross section (weak echo), respectively. The reader is cautioned to keep in mind while studying the images that our gray-scale rendering denotes radar cross section with stronger shading, so that "bright" features correspond to darker shading.

3.1. Tharsis/Olympus

Earlier CW radar observations indicated that the Tharsis region gives the strongest depolarized echoes from Mars and presumably contains the highest concentration of decimeter-scale roughness on the planet [*Harmon and Ostro*, 1985; *Thompson and Moore*, 1989]. This was confirmed by the VLA radar images [*Muhleman et al.*, 1991; *Butler*, 1994]. Our images show that the radar appearance of this region is complex and nonuniform. The only large, uniform expanse of enhanced depolarized echo is the east Tharsis plains. To the west, on the Tharsis ridge axis and Olympus Mons, the echo features are more distinct and localized. Although all of the major shields show radar-bright features or are the source of bright flows, they do not conform to any sort of regular or characteristic form in the radar images.

3.1.1. East Tharsis plains. The volcanic plains between Ascraeus Mons and Lunae Planum appear as a rather uniform expanse of moderately enhanced radar brightness (Figure 3; see also *Harmon* [1997b, Figure 14]). The eastern edge of the enhancement is well defined and coincides with the boundary between the Tharsis Montes volcanic plains (mostly unit At_5; see Plate 1) and the older (Hesperian) ridged plains of Lunae Planum. The brightest part of this boundary is located in the volcanic plains adjacent to the chaotic terrain at the head of Kasei Vallis. The radar-bright plains extend on to the south, forming a peninsular feature embaying Echus Chasma. The southern boundary west of Echus Chasma coincides fairly closely to the boundary between the Tharsis plains and the older Syria Planum and fractured terra to the south (compare with Plate 1). Within the Tharsis plains is a radar-dark region corresponding to Fortuna Fossae, an island of fractured terra (unit Hf; see Plate 1). The northern limit of the bright east Tharsis plains lies close to the 20°N latitude line, south of the Uranian shields. The Uranian shields themselves do not show bright radar features, except for a small bright area on the southwest flank of Uranius Patera. The extreme northeast corner of the Tharsis plains shows faint horn-like features from Kasei Vallis (see *Harmon* [1997b, Figure 14]).

3.1.2. Ascraeus Mons. On the western edge of the radar-bright east Tharsis plains lies a very bright oval feature associated with the Ascraeus Mons shield (see Figure 3 and Plate 2a). This feature is offset toward the southcentral part of the shield and has a radar-dark center that includes the caldera. The brightest part of this feature ($\sigma^o_{sc} = 0.211 = -6.38$ dB at $\theta = 30°$), located at 103.7°W, 9.1°N, is also the brightest point in Figure 3. The shield also shows a very bright feature in the Goldstone/VLA radar images [*Butler*, 1994; *Muhleman et al.*, 1995]. Running south of the shield is a bright "tail" that lies along the eastern edge of the volcano's southern flow fan. There is also a bright band extending northeast from the shield. The lower western side of the shield, as well as an extensive area west of the volcano, is radar dark. There is apparently a strong dichotomy between rough terrain on the east flank of the volcano and smooth terrain on the west flank. The center of the radar-dark side coincides with a young debris apron (unit As), which may be obscuring older radar-bright flows, although the mapped debris apron is much smaller than the dark area. Alternatively, the dark area may be associated with an effusive late-stage lava flow from the western flank of Ascraeus Mons [*Zimbelman et al.*, 1996] or the most northern of the volcanic ash deposits left by a late sequence of pyroclastic eruptions from the west flanks of all three Tharsis shields [*Edgett et al.*, 1996, 1997].

3.1.3. Pavonis Mons. The shield of Pavonis Mons is almost entirely radar dark. A faint summit ring of bright material around the caldera can barely be seen in Figures 3 and 7. The entire northern side of the shield, as well as the plains extending north and northwest of the shield, are radar dark. Part of the dark region northwest of the shield may represent obscuration of rougher surfaces by a debris apron (unit As in Plate 1), although the proposed west flank ash eruptions [*Edgett et al.*, 1996, 1997] may also be responsible. The lower eastern flank of the shield, along with plains to the east and northeast, make up a bright teardrop-shaped feature that corresponds to the Pavonis "east lava apron" discussed by *Hodges and Moore* [1994] (see Figure 3 and Plate 2a). This radar feature

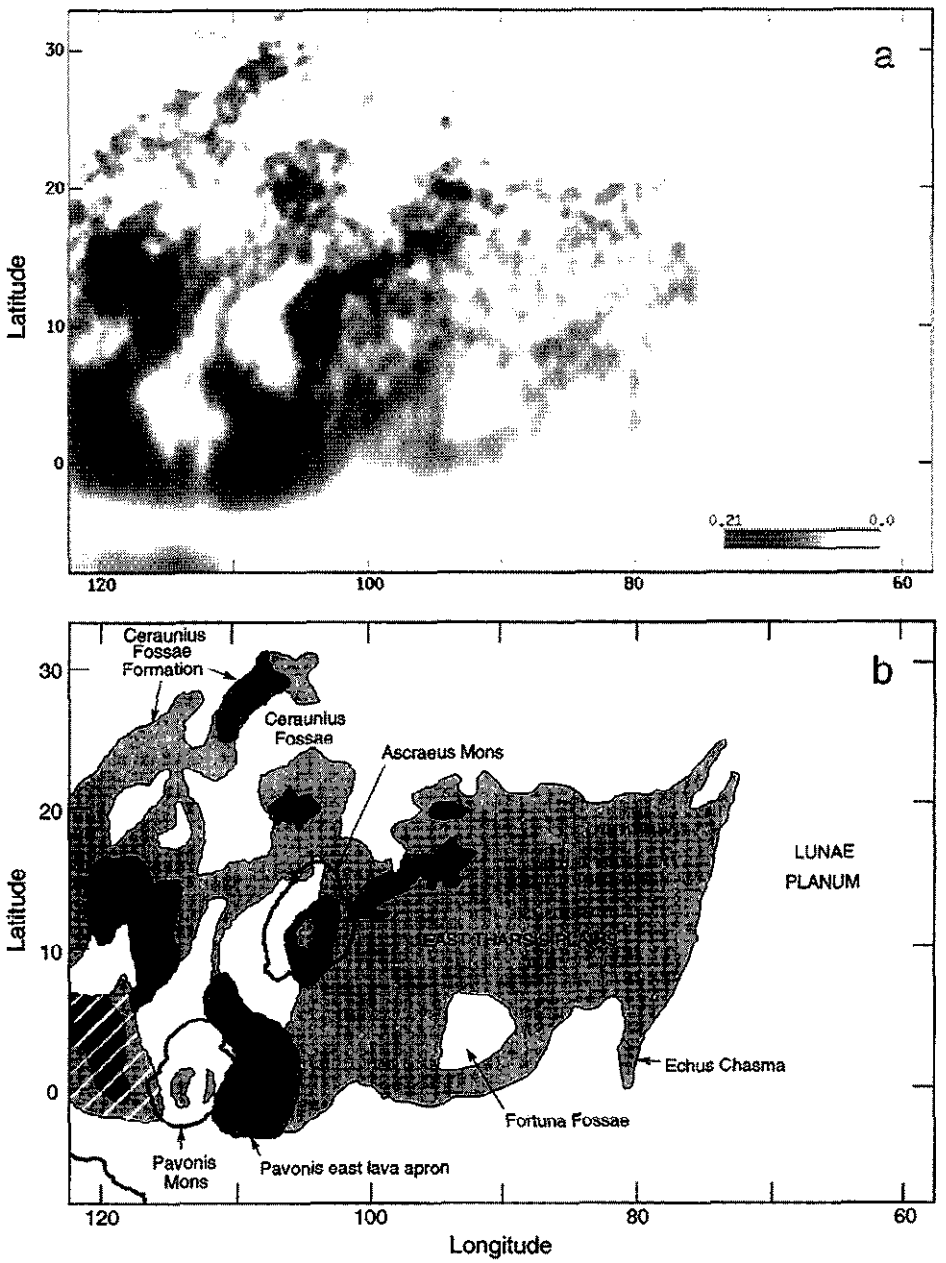

Figure 3. (a) Radar image of northeast Tharsis and environs. Darker shading corresponds to higher specific cross section σ^o_{sc}. The peak σ^o_{sc} in the image is 0.211 (on the southern part of the Ascraeus Mons shield). The image is a weighted average of images from five observing runs obtained on three separate dates between November 5 and December 16, 1990 (sub-Earth latitude = 4.8°S–12.1°S). The range of mean incidence angles is 6°–66° across the image. (b) Sketch map of the image showing the dominant features and their names. Edges of the major shields are indicated (thick lines). Areas with significant fold-over from the N/S ambiguity effect are identified (diagonal hatching).

is also prominent in the Goldstone-VLA images [*Butler*, 1994; *Muhleman et al.*, 1995]. The Pavonis east lava apron is apparently one of the largest expanses of rough lava surface on Tharsis. It is also a relatively young feature; *Hodges and Moore* [1994] place it as younger than the Pavonis Mons shield and contemporaneous with the Olympus Mons shield. From the north end of the teardrop runs a narrow, channel-like feature that merges with other bright features to the north and separates the dark region north of Pavonis Mons from the dark region west of Ascraeus Mons. The northern teardrop and "channel" coincide with mapped lava flows [*Hanley and Zimbelman*, 1995; *Mouginis-Mark et al.*, 1982] that flow north in a broad S curve out of the east lava apron.

3.1.4. Arsia Mons. Arsia Mons and southern Tharsis are covered by the images in Figure 4 and Plate 2b. The Arsia Mons shield has an extremely bright col-

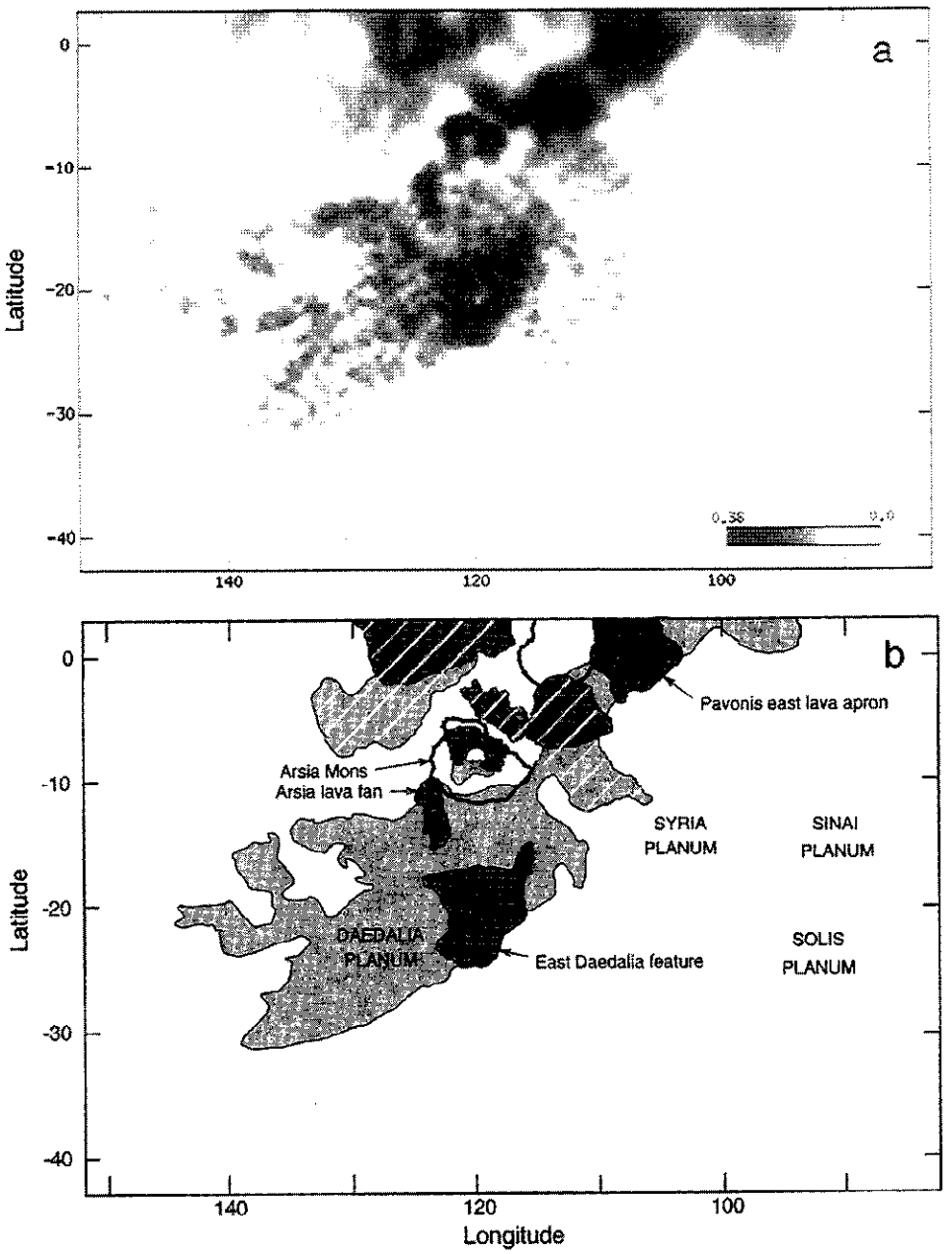

Figure 4. (a) Radar image of southern Tharsis and environs. The peak σ^o_{sc} in the image is 0.363 (on the northern part of the Arsia Mons shield). The image is a weighted average of images from five observing runs on December 27, 1992 (sub-Earth latitude = 9.3°N). The range of mean incidence angles is 8° 65°. (b) Sketch map corresponding to this image. Edges of the major shields are indicated (thick lines). Areas with significant fold-over from the N/S ambiguity effect are identified (diagonal hatching).

lar around the northern side of the caldera. With a peak σ^o_{sc} of 0.363 (=−4.4 dB at θ = 19°) at 118.4°W, 7.6°S, this is the brightest feature that we have found on Mars. The caldera and southern half of the shield are much darker. Other areas around the shield, including a debris apron, are radar dark. Just to the southwest of the shield is a bright feature that corresponds to the south lava fan. A similar feature just northeast of the shield may be coming from the north lava fan, although here there is some confusing fold-over from the Ceraunius Fossae Formation. South and southwest of Arsia Mons is a vast radar-bright feature occupying Daedalia Planum. This is also the most prominent bright feature in the Goldstone/VLA images [*Muhleman et al.*, 1991; *Butler*, 1994]. The brightest portion of the Daedalia feature in the Arecibo image is centered near 120°W, 20°S; we label this the "east Daedalia feature" in Figure 4b. The lava flows in this area have a very distinctive appearance in the Viking images, showing strong albedo streaks (Figure 5a) and well-defined flow fronts (Figure 5b). The eastern edge of the east Daedalia feature is very well defined and coincides precisely with the point

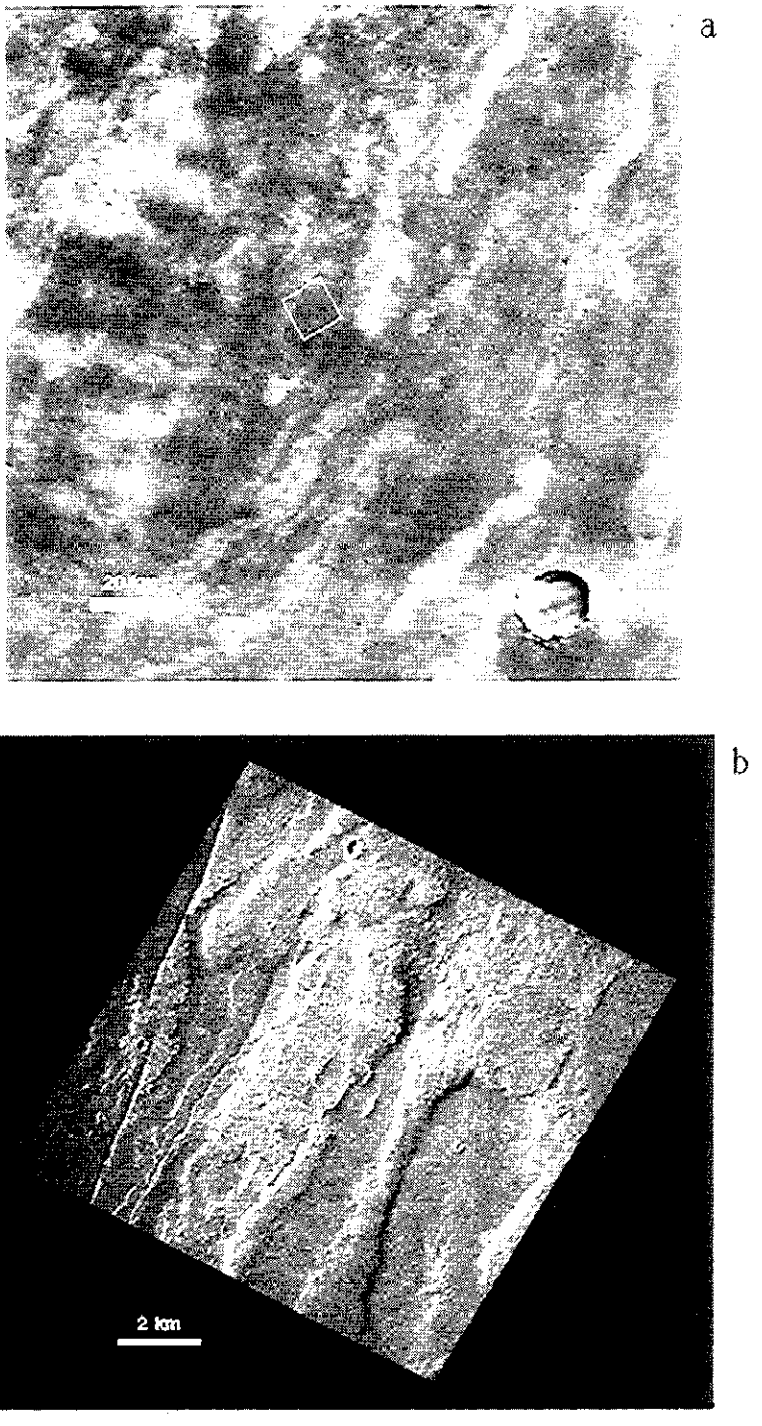

Figure 5. (a) Viking medium-resolution visible image mosaic of a western portion of the "east Daedalia" feature. The location is given by a box in Plate 2b. The entire image is located within unit At_5 of the Tharsis Montes Formation. Note the prominent albedo streaking associated with lava flows. (b) Viking high-resolution visible image of the region inside the box shown in Figure 5a. Note the prominent lava flow fronts.

where radar scattering profiles show a dramatic increase in quasi-specular roughness [*Schaber*, 1980]. Apparently, this region is very rough on a wide range of spatial scales. Most of the Daedalia feature (including east Daedalia) is mapped as lava flows of the At_5 unit (Plate 1). Figure 6a shows a histogram of σ^o_{sc} computed from the entirety of the south Tharsis image (Figure 4), as well as from that portion of the image (south of 10°S latitude) that is designated as unit At_5 in the geologic map. This shows a very high average radar brightness of σ^o_{sc}=0.21 (−6.8 dB) for this unit.

3.1.5. Other Tharsis features. The region of northern Tharsis between the Tharsis ridge and Olympus Mons shows complex radar-bright structure (Figure

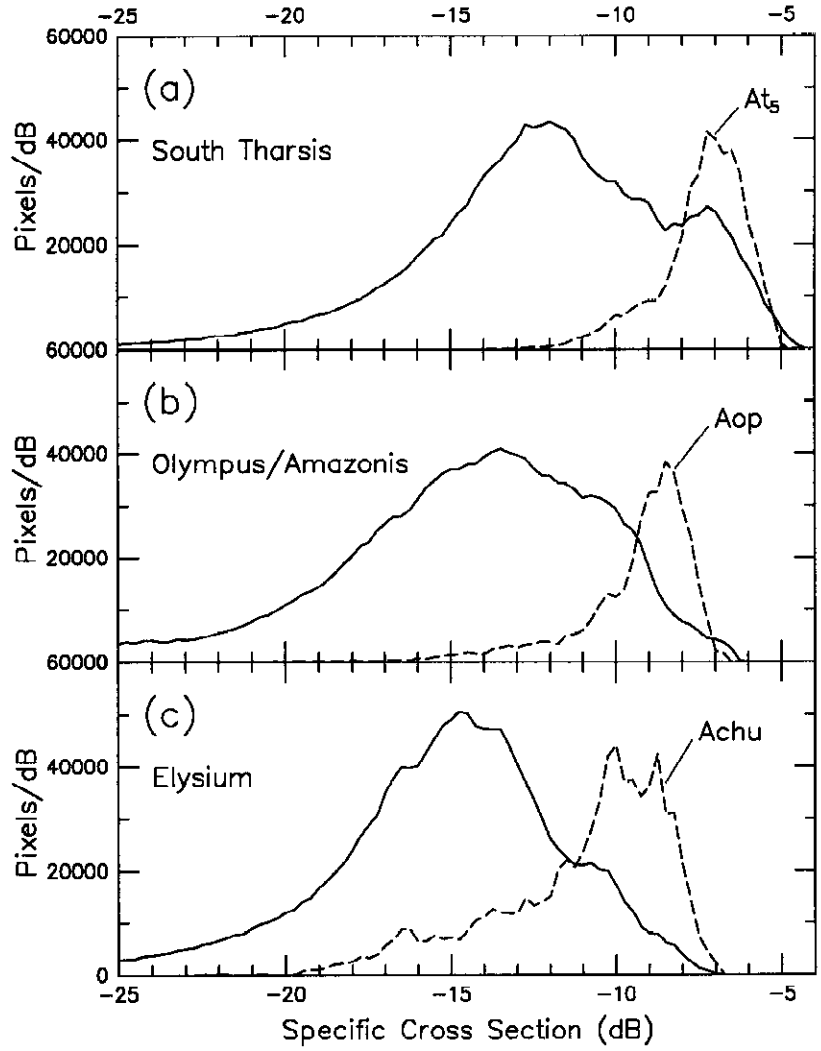

Figure 6. Histograms of σ^o_{sc} for the following areas: (a) the entire image in Figure 4a (solid line) and the portion of that image (south of 10°S latitude) classified as unit At_5 (dashed line); (b) the entire image in Figure 7a (solid line) and the portion of that image classified as unit Aop (dashed line); (c) the entire image in Figure 10a (solid line) and the portion of that image classified as unit Achu (dashed line). The vertical scales refer to the solid lines; the dashed lines have been scaled up by a factor of 10 in Figures 6a and 6c and by a factor of 5 in Figure 6b.

3). Due north of Ascraeus Mons is a large circular feature (centered near 104°W, 20°N) that butts up against Ceraunius Fossae to the north. This bright basin connects with the bright Tharsis plains to the southeast and with sinuous curved features to the southwest (one of which comes out of the Pavonis lava apron). Since the lava flow directions in these features are toward the north, it is possible that the feature south of Ceraunius Fossae is a catch basin for north flowing lavas, although grabens and fissures in the center of the feature may also be local sources of radar-bright lavas. The higher, older fractured terra (unit Nf; see Plate 1) of Ceraunius Fossae is radar dark, as are the plains and shields to its east. North of Ceraunius Fossae is a bright feature that coincides with the Ceraunius Fossae Formation (unit AHcf; see Plate 1), a region of many small volcanic shields and fissure-fed flows [*Scott and Tanaka*, 1986; *Hodges and Moore*, 1994]. The Ceraunius Fossae Formation is relatively young; *Hodges and Moore* [1994] place it as contemporaneous with late-stage volcanism from the main Tharsis shields. The feature connects with the Olympus lava apron to the west (Figure 7). The region north of the Ceraunius Fossae Formation is relatively dark, with no obvious radar feature seen coming from Alba Patera (see the NE corner of Figure 7a). *Butler* [1994] noted a similar lack of an Alba Patera feature in the VLA images, which he attributed to degradation of volcanic roughness over the age of this relatively old volcano. Finally, there is a very prominent feature at 118°W, 13°N (midway between Ascraeus and Olympus Mons) that butts up against Ulysses Fossae to the west. This feature curls around from the south in a manner suggesting it is a catch basin for north flowing lavas, which would be consistent with the flow direc-

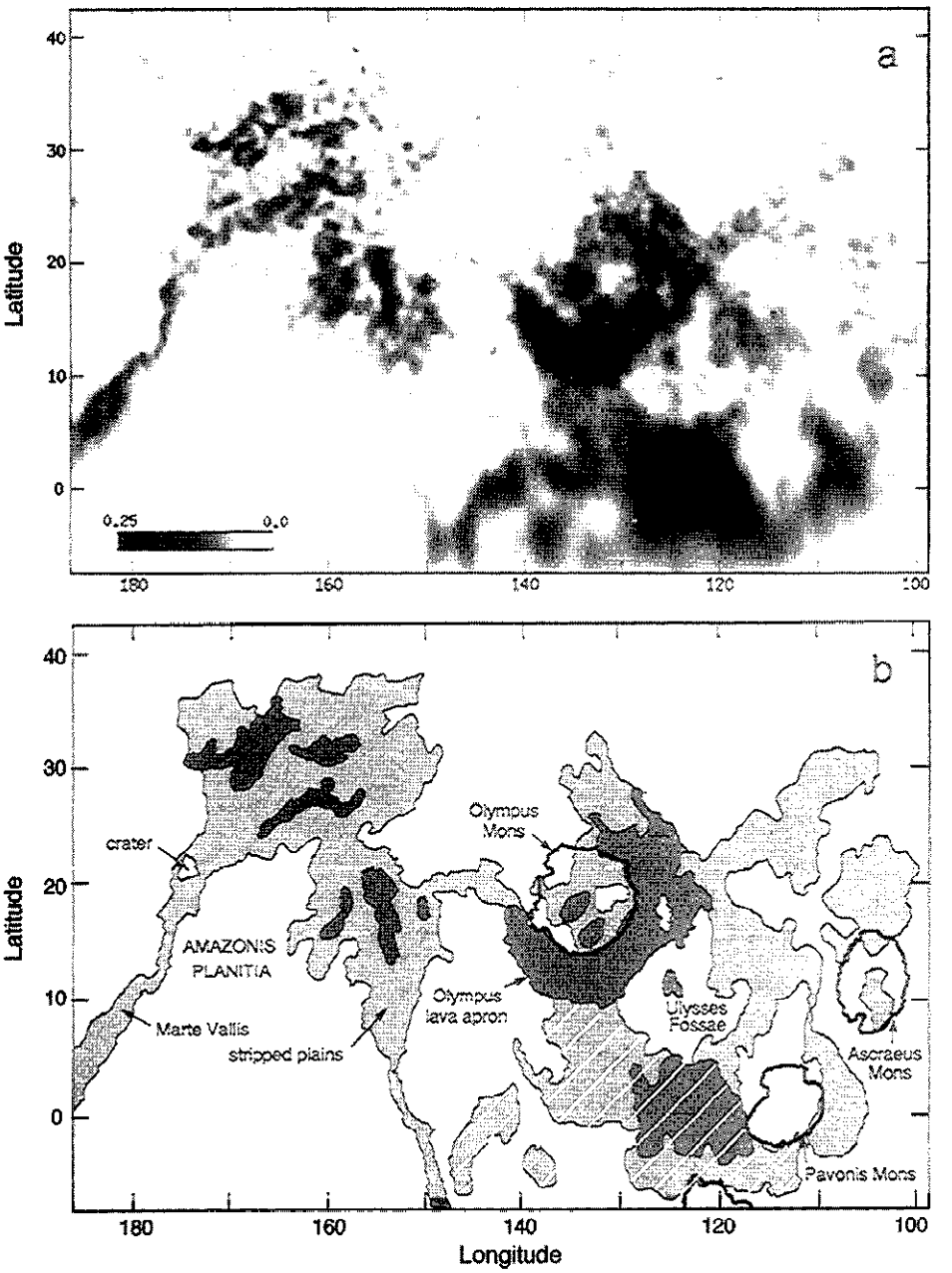

Figure 7. (a) Radar image of the Olympus/Amazonis region and environs. The peak σ^o_{sc} in the image is 0.254 (at the western end of the "Olympus lava apron"). The image is a weighted average of images from five observing runs on December 6, 1990 (sub-Earth latitude = 10.7°S). The range of incidence angles is 7°–70°. (b) Sketch map corresponding to this image. Edges of the major shields are indicated (thick lines). Areas with significant fold-over from the N/S ambiguity effect are identified (diagonal hatching)

tions deduced by *Mouginis-Mark et al.* [1982]. This same feature can be seen in the Goldstone/VLA images [*Butler*, 1994; *Muhleman et al.*, 1995]. Ulysses Fossae itself (see Figure 7), like Ceraunius Fossae, is a topographically high, radar-dark region of fractured terra (unit Hf; see Plate 1).

3.1.6. Olympus Mons. The Olympus Mons region is covered by the images in Figure 7 and Plate 2c. The dominant bright feature in the Olympus Mons area is not the shield itself but, rather, a crescent-shaped feature that wraps around the southern and eastern sides of the shield and which we will refer to informally as the "Olympus lava apron." This feature corresponds very closely to unit Aop, the Olympus Mons plains member (see Plate 1). The brightest part of this feature is located at 138.4°W, 13.9°N (σ^o_{sc} = 0.254 = −6.0 dB at θ = 27°). The histogram in Figure 6b shows the Aop unit to have an average σ^o_{sc} of 0.14 (−8.6 dB). This unit

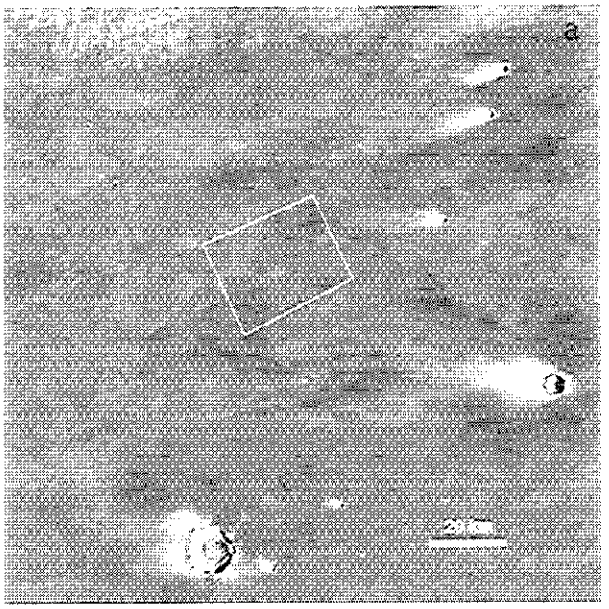

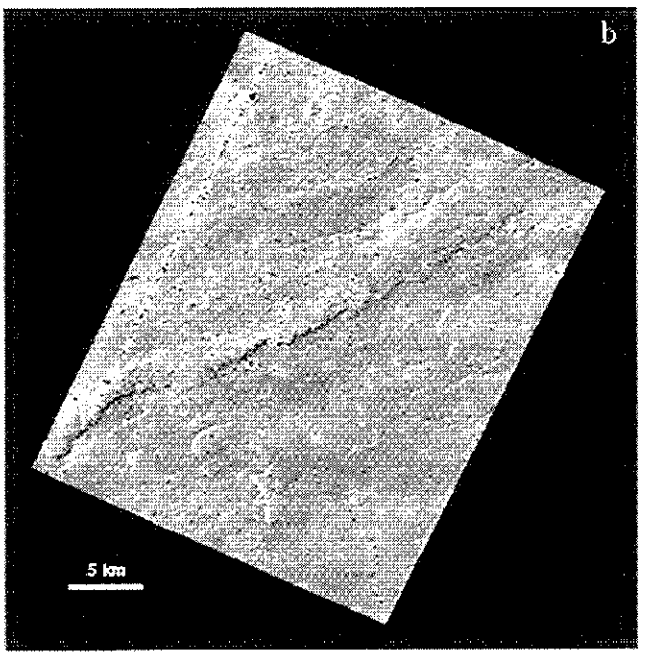

Figure 8. (a) Viking medium-resolution visible image of the Olympus lava apron (see location box in Plate 2c). This terrain is primarily of unit Aop, with some unit Aos in the NW corner. (b) Viking high-resolution visible image of the region inside the box shown in Figure 8a. Note the prominent lava flow fronts.

contains the youngest lava flows in the Olympus Mons region. These flows show numerous well-preserved flow fronts, examples of which can be seen in the Viking image in Figure 8. This contrasts with the more subdued appearance of surrounding older units. Part of the radar apron feature also includes off-shield flows of unit Aos (the Olympus Mons shield member). Much of the shield itself is dark by comparison, although two bright knots can be seen near the summit and on the lower southern flank. It is interesting to note that at least part of the caldera is radar bright, in contrast to the Tharsis calderas. The eastern, northwestern, and southwestern parts of the shield appear dark and are presumably smoother than other areas of the volcano. The aureole north and west of the volcano is almost uniformly radar dark; a small island of aureole material can even be seen as a dark patch inside the bright lava apron due east of the shield. The aureoles apparently have a much smoother small-scale texture than do the younger apron and shield flows, despite their chaotic appearance in orbiter images.

3.2. Amazonis

3.2.1. Amazonis bright areas. CW observations indicated that there is a depolarized enhancement at the Amazonis longitudes between Tharsis and Elysium [*Harmon and Ostro*, 1985], and the VLA maps confirmed the existence of a feature in northern Amazonis [*Muhleman et al.*, 1991]. The Amazonis enhancement shows up well in Figure 7 (see also Figure 10). This feature coincides closely with the unit Aa_3 flows of the Arcadia formation (Plate 1). The Amazonis feature actually appears to be made up of northern and southern sections, which are connected near 159°W, 23°N. The northern section merges with the Marte Vallis outflow channel feature. It has been suggested that the north Amazonis flows represent lavas that debouched from Marte Vallis [*Plescia*, 1990; *Harmon et al.*, 1992b]. This is in apparent contradiction with the age sequence of *Scott and Tanaka* [1986], who place the Aa_3 formation (mid-Amazonian) as older than the channel (late Amazonian). Also unclear is whether the northern and southern parts of the Amazonis feature are related or are merely contiguous. Support for separate origins comes from (1) the narrowness of the contact between the northern and southern features and (2) the fact that much of the southern feature has been mapped separately as eroded stripped plains [*Schultz and Lutz*, 1988].

3.2.2. "Stealth" and Medusae Fossae Formation. One of the most interesting results from the Goldstone/VLA imaging [*Muhleman et al.*, 1991] was the discovery of an extremely radar dark region extending west of southern Tharsis and into southern Amazonis. This feature, dubbed "Stealth" by its discoverers, showed no detectable depolarized echo in the VLA images, implying a smooth and/or low-density surface layer devoid of buried scatterers. *Muhleman et al.* [1991] and *Butler* [1994] suggested that the Stealth materials are pyroclastic deposits from the Tharsis volcanoes. This idea was motivated by the fact that a portion of the Stealth region coincides with the Medusae Fossae Formation (Figure 9b), which *Scott and Tanaka* [1982] had claimed to be composed of welded ash flow tuffs (ignimbrites). *Edgett et al.* [1997] recently reexamined the pyroclastic hypothesis, arguing that the

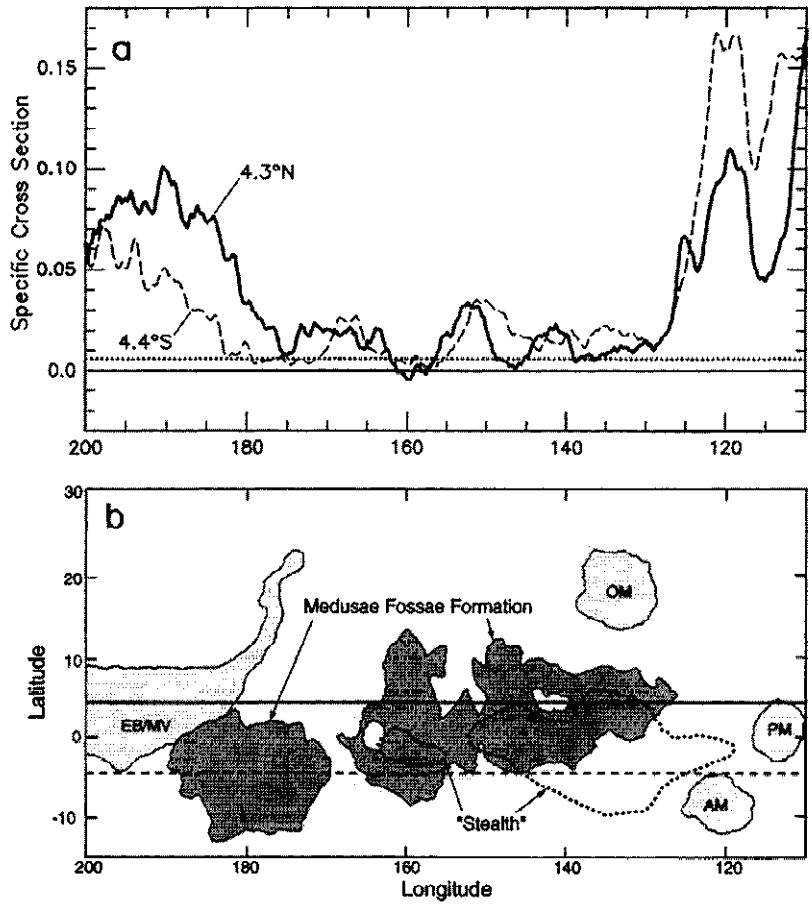

Figure 9. (a) Normal-incidence radar cross-section [$\sigma^o_{sc}(\theta = 0)$] computed along the two radar tracks shown on the map. The radar footprint is $\pm 5°$ of latitude centered on the sub-Earth track. Also shown is the $\sigma^o_{sc}(0) = 0.006$ cross section threshold for the Stealth feature from *Edgett et al.* [1997]. (b) Map showing the sub-Earth radar tracks for November 2, 1990 (dashed line) and January 28, 1993 (solid line). Also shown are the Medusae Fossae Formation (shaded areas) as mapped by *Scott and Tanaka* [1986] and the $\sigma^o_{sc}(0) = 0.006$ contour for Stealth (dotted shapes). Other features are the Elysium Basin and Marte Vallis (EB/MV) and the Olympus Mons (OM), Pavonis Mons (PM), and Arsia Mons (AM) shields.

Stealth deposits are loose, wind-blown, volcanic tephra that were deposited on the Medusae Fossae Formation, as well as on lava flows outside Medusae Fossae, thus weakening any direct connection between Stealth and the underlying consolidated or welded material making up the Formation.

We were interested in determining if Stealth also appeared dark to the Arecibo radar, since the longer S-band wavelength could be expected to give much deeper penetration through any radar-absorbing surface layers. The image in Figure 7, which was obtained from 1990 data with a sub-Earth latitude of 10°S, does appear radar dark over the Stealth region. The radar-dark region can be seen to extend as far as 12°N on both sides of the southern Amazonis bright feature, in good agreement with the northern extension of the Medusae Fossae Formation but somewhat north of the main part of Stealth as mapped by *Edgett et al.* [1997] (see Figure 9b). However, getting a quantitative measure of the S-band Stealth from the image in Figure 7 is problematic owing to the N/S ambiguity effect and the difficulty of delay-Doppler imaging near the Doppler equator. Therefore we have done a special analysis to estimate the depolarized echo strength along two separate tracks crossing the Medusae Fossae Formation and the "Greater Stealth" region (see the map in Figure 9b). It was noticed that the delay-Doppler arrays obtained along these tracks showed "holes" at their leading edges, suggesting complete dropouts in detectable echo power. This is quantified in Figure 9a, which shows profiles of the leading-edge echo strength expressed as a normal-incidence reflectivity $\sigma^o_{sc}(\theta = 0)$ to permit direct comparison with the VLA measurements. This reflectivity represents an average over a 10°-wide latitude footprint centered on the sub-Earth track. Figure 9 shows a very close correspondence between dropouts of echo power and those places where the $\pm 5°$ radar footprint is mostly or entirely within the Medusae Fossae Forma-

tion. The correspondence between echo dropouts and Stealth is not as strong, as can be seen from the non-negligible echo along the southern track at 135°W longitude, where the radar footprint is entirely within the Stealth contour (Figure 9b). Clearly, there is a much stronger association between our S-band Stealth feature and the Medusae Fossae Formation than was found to be the case by *Edgett et al.* [1997] for the X-band Stealth feature in the VLA images. The greater penetrating power of the S-band radar may account for some of this difference. Apparently, the underlying consolidated material of the Medusae Fossae Formation (and not just a loose tephra cover) is "stealthy" at 12.6 cm, which is what one might expect if the formation consists of thick, homogeneous deposits of welded tuff with smooth surfaces and a paucity of embedded rocks.

3.3. Elysium

Elysium is the second great Mars volcanic province after Tharsis and, like Tharsis, was known to have a depolarized radar enhancement based on CW data [*Harmon and Ostro*, 1985]. Only a small portion of Elysium was visible in the 1988 VLA images [*Muhleman et al.*, 1991], and the first image covering the entire region was obtained from the 1990 Arecibo CLP observations. A preliminary Elysium image and a discussion of the intriguing radar appearance of this region are given by *Harmon et al.* [1992b]. Because of multirun averaging, the new Elysium image (Figure 10; see also Plate 2d) is of better quality than that shown by *Harmon et al.* [1992b]. This image is essentially free of some of the N/S ambiguity fold-over that affects parts of the Tharsis images, since the southern ambiguity points were located entirely in the radar-bland cratered highlands.

3.3.1. Elysium volcanoes. Elysium Mons is the only volcano in this region showing a prominent radar-bright feature. As with the Tharsis volcanoes, the Elysium Mons enhancement is irregular and asymmetric, being concentrated on the east and southeast sides of the shield (see Figure 10b and Plate 2d). Hecates Tholus shows only a small feature on its south flank, while Albor Tholus cannot be distinguished from the general enhancement southeast of Elysium Mons. The lack of strong features from these two volcanic tholi may be related to their great ages. A small, bright feature can be seen midway between Elysium Mons and the northern Amazonis feature at 188°W, 25°N. This feature is located in a complex region of Elysium volcanic plains and knobby terrain and corresponds to no known volcanic edifice.

A bright band can be seen extending east-southeast of Elysium Mons. The trend of this "ESE band" feature aligns with the direction of lava flows radiating southeast of Elysium Mons. There may be some association between this extended band and the bright patch located on the southeast side of the Elysium Mons shield. Viking images show well-defined lava flows within this band. Many flows have also been identified west of Elysium Mons [*Mouginis-Mark et al.*, 1984], but, apparently, they are not as rough as the flows to the east. Most of the ESE band is separated from the Elysium Basin feature to the south by a wedge of radar-dark terrain. Part of this terrain lies in the classical Cerberus low-albedo feature known from old telescopic observations. If the Cerberus dark band is a sand sheet, as has been proposed, then it is possible that there are rough flows between the ESE band and the Elysium Basin that are obscured by radar-absorbing sand.

The VLA coverage of the Elysium region was completed with the addition of observations during the 1992–1993 opposition [*Butler*, 1994; *Muhleman et al.*, 1995]. A comparison with the CLP image shows some interesting differences between the X-band and S-band images in the vicinity of the Elysium shields. For example, the prominent bright feature that we see on the southeast side of the Elysium Mons shield is not seen in the VLA images. Also, the ESE band is the dominant bright feature in the VLA Elysium images, which is not the case at S-band.

3.3.2. Elysium Basin and Marte Vallis. The largest single bright area in our image of the Elysium region is the Elysium Basin, located southeast of Elysium Mons and north of the cratered highlands. The eastern side of this enhancement narrows into a sinuous feature that corresponds to the youngest outflow channel on Mars. Although this channel is sometimes referred to informally as the Amazonis Channel [*Hodges and Moore*, 1994], we will adopt the newer "Marte Vallis" designation [*Golombek et al.*, 1997]. The Marte Vallis channel is probably the single most distinctive feature in all of our images (see Figure 10 and Plate 2d, as well as the western edge of Figure 7). The channel shows up as being brighter than the basin from which it emerges. It appears to have its source just east of the center of the basin feature and just south of the Cerberus Rupes fractures; this source region can be seen in the Viking image in Figure 11a. Here one sees the channel flowing around the south side of two inselbergs before continuing on to the northeast. At the 180°W meridian the channel narrows, doglegs east, and then turns north. This narrow, kinked part of the channel can be seen as the dark feature at the top of Figure 11b, just southeast of Orcus Patera. Continuing north, the channel flows around a crater at 174°W, 21°N; the splitting of the flow by the crater can clearly be seen in the radar image (Figure 10). Beyond the crater the feature spreads out, as if debouching into northern Amazonis (as discussed in section 3.2.1). The narrow part of the Marte Vallis channel (outside Elysium Basin proper) does not show up in the VLA images [*Butler*, 1994; *Muhleman et al.*, 1995], which must be due, at least in part, to the lower resolution. The VLA images do show the enhancement from the Elysium Basin, including the bright regions on its eastern edge (where Marte Vallis flows) and southern tip, though none of these areas is as bright as their ESE band feature.

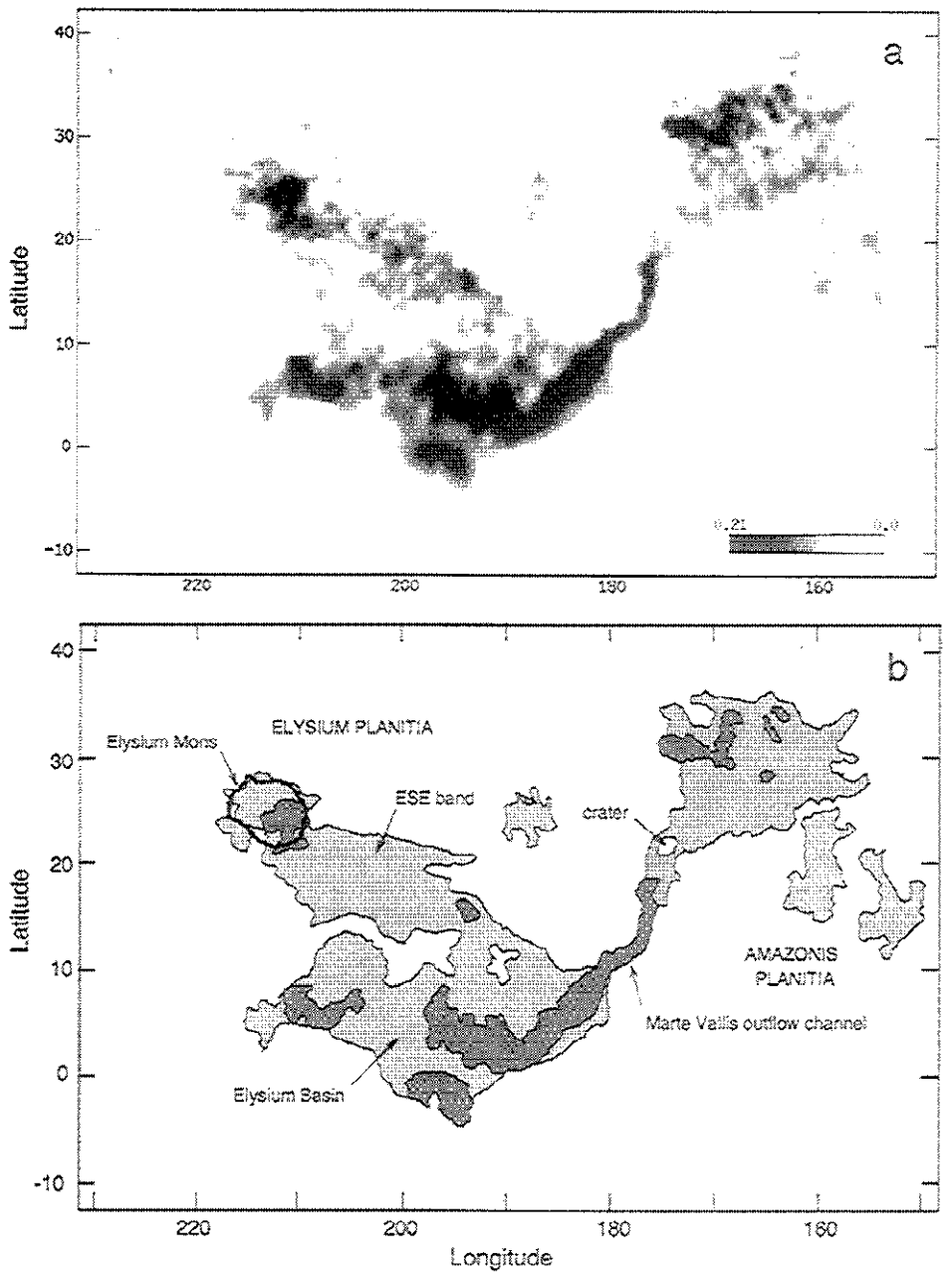

Figure 10. (a) Radar image of the Elysium region and environs. The peak σ^o_{sc} in the image is 0.209 (in the Marte Vallis channel). Most of the image is a weighted average of images from three observing runs on December 1, 1990 (sub-Earth latitude = 9.7°S). The NE corner of the image (NE of 180°W, 20°N) is from three runs on December 20, 1992 (sub-Earth latitude = 10.6°N). The range of incidence angles is 4°–70°. (b) Sketch map corresponding to the image in Figure 10a.

The entire basin/channel complex is mapped as unit Achu ("channel and flood plain") in Plate 1. This late Amazonian formation may be the youngest surface on Mars. The histogram in Figure 6c shows that the Achu unit is nearly as bright, on average, as unit Aop in the Olympus lava apron. The brightest part of the image in Figure 10 is located at 184.1°W, 5.9°N in the Marte Vallis channel (σ^o_{sc} = 0.209 = −6.8 dB at θ = 19°). Marte Vallis is unique in being the only outflow channel showing a strong radar feature. Some of the Chryse channels show modest SC enhancements [*Harmon*, 1997b], but these have only a third of the brightness of Marte Vallis. The obvious question to be asked is why a fluvial/lacustrine region such as this should give such a bright depolarized feature. One possibility is that the basin/channel floor is actually surfaced with rough lava flows such as those thought to be responsible for the Tharsis/Olympus bright features. A lava fill has, in fact, been proposed by *Plescia* [1990], who argued that extrusive volcanism accompanied (and possibly triggered) the water release that formed the lacustrine basin and outflow channel. There is a very close

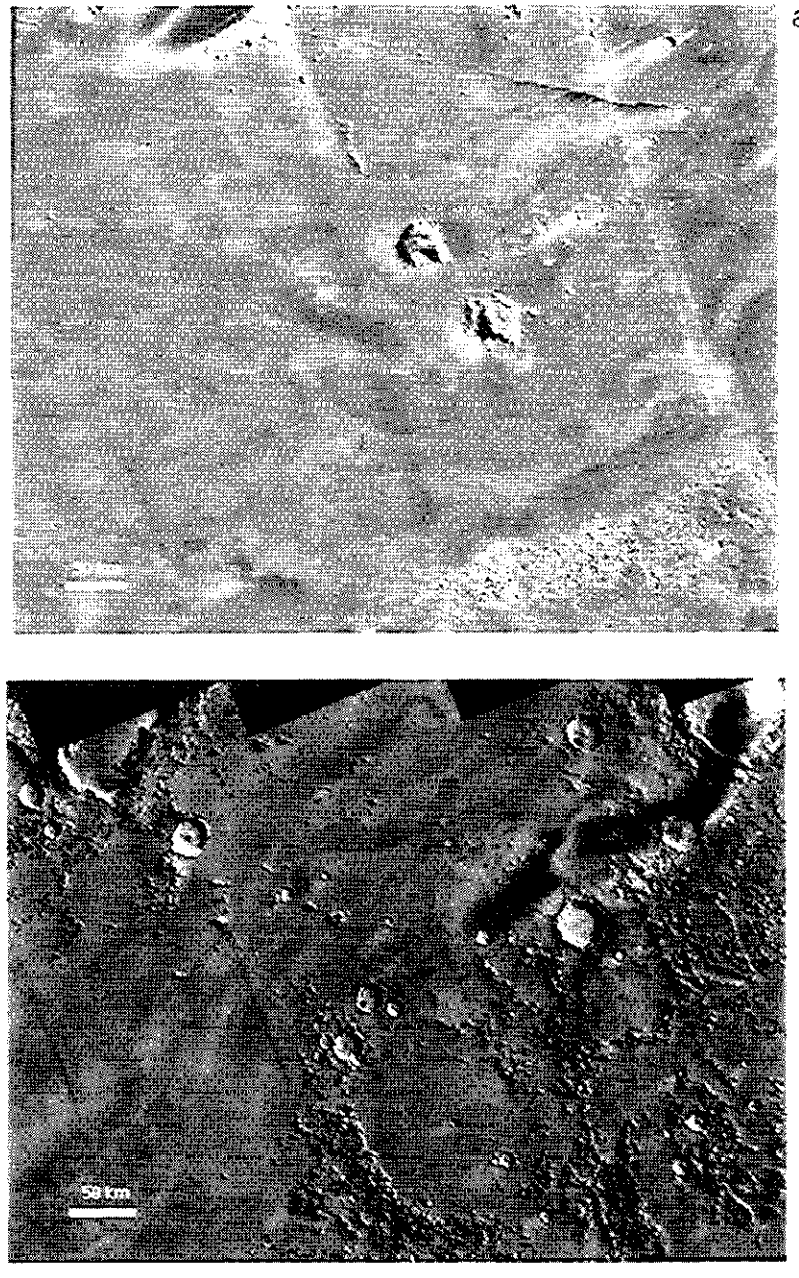

Figure 11. (a) Viking visible image mosaic corresponding to the left-hand box in Plate 2d. The Marte Vallis source region just SW of the two inselbergs and the section of main channel in the top right corner give the the strongest radar backscatter of the entire Elysium region. (b) Viking visible image mosaic corresponding to the right-hand box in Plate 2d. The Marte Vallis channel shows up as the darker streaks extending from the left edge to the top center. This entire portion of the channel (unit Achu) gives strong radar backscatter. The southern end of Orcus Patera is visible in the top left corner.

correspondence between our basin/channel feature and the volcanic "Cerberus Formation" mapped by *Plescia* [1990] [see also *Harmon et al.*, 1992b]. Also, the bright region near 195°W, 2°S at the southern tip of the basin (see Figure 10 and Plate 2d) corresponds to a region where *Schaber* [1980] identified lava festoons. On the other hand, *Scott and Chapman* [1991] mapped the basin/channel floor as a mix of volcanic and sedimentary units, so we cannot rule out the possibility that some of the apparent roughness of this surface is associated with fluvial erosion and deposition.

4. Discussion: Interpretation of Radar Brightness

The results from the Arecibo and Goldstone/VLA images confirm earlier speculation, based on CW spectra, that much of the enhanced radar backscatter from

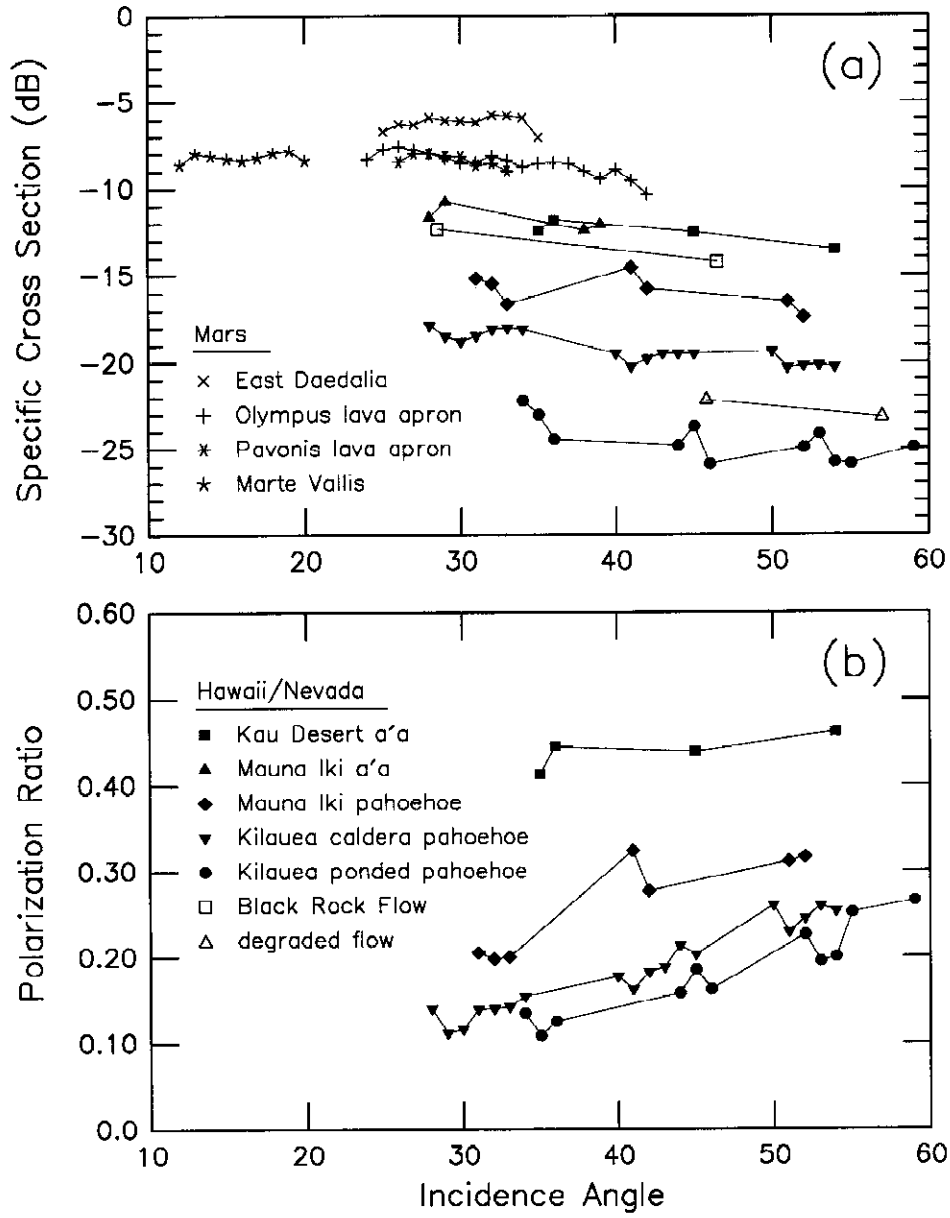

Figure 12. (a) Specific cross sections $\sigma^o_{sc}(\theta)$ versus incidence angle θ for bright radar features on Mars (skeletal symbols) and for terrestrial lava flows in Hawaii (solid symbols) and the Lunar Crater Volcanic Field in Nevada (open symbols). (b) Circular polarization ratios $\mu_c = \sigma^o_{sc}/\sigma^o_{oc}$ for the Hawaiian flows shown in Figure 12a.

Mars is associated with lava flows. It is worth considering, then, (1) how the absolute radar cross sections measured for the bright flows on Mars compare with radar results for terrestrial flows and (2) what this implies for the surface textures of the Martian lavas.

The histograms in Figure 6 show that the younger lava flows on Mars tend to have σ^o_{sc} in excess of 0.10 (−10 dB). The roughest terrestrial flows, on the other hand, tend to have σ^o_{sc} values below −10 dB. This difference can be clearly seen from Figure 12a, which shows $\sigma^o_{sc}(\theta)$ values measured for the brighter Martian features (east Daedalia, Marte Vallis, and the Olympus and Pavonis lava aprons) along with airborne synthetic aperture radar data from lava flows in Hawaii and the Lunar Crater Volcanic Field in Nevada. The Martian cross sections are even significantly higher than those for the extremely rough Hawaiian a'a flows. There is strong evidence that this difference between the Martian and terrestrial SC echo strengths may be associated more with a higher degree of depolarization (as expressed in the polarization ratio $\mu_c \equiv \sigma^o_{sc}/\sigma^o_{oc}$) than with higher total (OC + SC) diffuse cross sections. CW radar results [*Harmon et al.*, 1982; *Harmon and Ostro*, 1985; *Moore and Thompson*, 1991] indicate that some of the brightest Martian radar features must have diffuse μ_c values approaching (and possibly exceeding)

1.0, whereas the Hawaii flow data in Figure 12b show $\mu_c \leq 0.5$ [see also *Campbell et al.*, 1993]. It would appear likely, then, that the brightest Martian flows are characterized by higher levels of multiple scattering than are rough terrestrial flows. There are several possibilities for why this might be the case. First, Martian lava flows may simply have a more chaotic texture than their terrestrial counterparts. Although this might seem hard to imagine given the extreme roughness of some of the terrestrial flows used in Figure 12, it is possible that exotic rheology or lower gravity produces flows of spectacular roughness on Mars. In fact, *Wilson and Head* [1994] calculate that the growth rate of folds on flow surfaces should be 40% greater on Mars than on Earth. One might also expect a higher degree of multiple scattering if the Martian flows are blockier than the Hawaiian flows and more like SP flow, a blocky andesite lava deposit in northern Arizona for which *Campbell et al.* [1993] found μ_c values exceeding 1.0. Another possibility is that the Martian lavas have relatively high dielectric constants, resulting in high single-scattering albedos and enhanced multiple scattering. Finally, there is the possibility that the Martian flows give rise to some form of volume scattering not normally seen on Earth. This might be the case if, for example, the flow texture were so frothy as to contain internal scattering voids within a few wavelengths of the surface. Alternatively, the flow surface might be a mixture of dust and volume scatterers in the form of embedded volcanic rocks. Although flows covered with 1 to 3 m of aeolian dust can be found in the Mojave and Nevada deserts, the presence of desert pavements at the surface and 1–3% (or more) moisture in the dust prevents volume scattering within these flows [*Arvidson et al.*, 1993]. On Mars, desert pavement formation may be precluded by a lack of cobble-sized rocks and the regular freeze-thaw cycle that plays a role in keeping cobbles at the surface on Earth. Martian soils should also be drier than terrestrial dust deposits. Both differences would provide a low-loss regolith more conducive to multiple volume scattering. If the losses are sufficiently low, the volume scattering could include a significant contribution from "coherent backscatter," the mechanism thought to be responsible for the strong, highly depolarized echoes from the Galilean satellites and Mars' southern ice cap (see next section). The low thermal inertias measured over Mars' volcanic provinces indicate a substantial dust cover in these regions. If this dust forms homogeneous mantles covering monolithic flows, then there will be no enhanced multiple scattering and echoes from the buried interface will be preferentially attenuated at shorter wavelengths; a wavelength dependence consistent with this scenario has, in fact, been observed [*Harmon et al.*, 1992a]. Alternatively, the dust mantle could contain suspended rocks or blocks if the flow emplacement was followed by episodes of mass wasting ("rubbling"), impact gardening, and dust deposition. The relative dryness and slowness of weathering on Mars would tend to preserve the integrity of a regolith of blocks and loose dust by inhibiting those processes that produce duricrust and desert pavement on the Earth. Whether such a regolith would give echoes with the observed wavelength dependence depends on the size distribution of the entrained rocks, where the rocks are placed within the dust mantle, and the loss tangent of the dust.

Our radar images show that the volcanic provinces contain radar-dark regions as well as the bright features just discussed. Most of these dark features are associated with debris fans (aureoles), ash flows, or fractured remnants of highland terra. Ash flows, such as those that have been proposed for Stealth and the late west flank eruptions from the main Tharsis shields, are certainly plausible candidates for radar-absorbing features, given the depth and homogeneous texture of such deposits on Earth. Ash flows and young aureoles may well be obscuring older, rougher volcanic flows. Older aureoles and fractured terrae would tend to retain their intrinsic radar-dark appearance because they are topographic highs, protruding as islands above the younger, rougher flows.

5. Polar Ice Caps

The Goldstone/VLA images [*Muhleman et al.*, 1991; *Butler*, 1994] showed a strong, highly depolarized feature centered on the south polar residual ice cap. This discovery and the subsequent discoveries of similar features from putative ice deposits at the poles of Mercury [*Slade et al.*, 1992; *Harmon and Slade*, 1992; *Butler et al.*, 1993; *Harmon et al.*, 1994b] suggested that enhanced radar backscatter is a common property of planetary ices and not just a peculiarity of the icy Galilean satellites. The similarity of the anomalous echoes from Mars, Mercury, Europa, Ganymede, and Callisto suggests that a common mechanism is at work, possibly some form of multiple volume scattering in a low-loss ice regolith such as the "coherent backscatter" mechanism of *Hapke* [1990]. The Martian ice caps are especially important in this context, since they are good candidates for future bistatic radar, radio sounding, and surface-sampling experiments using spacecraft orbiters and landers. Here we present some new results on the radar properties of Mars' south and north polar ice caps based on a comparison of the Arecibo CLP data with Arecibo CW, Goldstone CW, and Goldstone/VLA results.

5.1. South Polar Cap

Southern sub-Earth latitudes made Mars' south pole visible to the Arecibo radar during 1988 CW and 1990 CLP observations. It was expected that a strong 12.6-cm radar anomaly would be found similar to that seen in the 3.5-cm images. Instead, we found a relatively weak feature, indicating that the south polar anomaly is strongly wavelength dependent. We base this con-

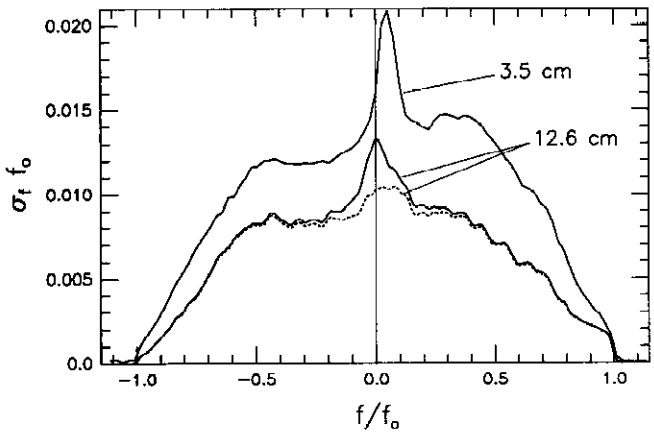

Figure 13. Radar Doppler spectra (solid lines) of the Mars depolarized (same-sense circular polarization (SC)) echo from Arecibo (λ=12.6 cm) and Goldstone (λ=3.5 cm) observations during the 1988 opposition. The mean sub-Earth points are 311°W, 25.1°S (3.5 cm) and 313°W, 20.3°S (12.6 cm). Also shown is the 12.6-cm spectrum with a 0.6% polarization cross-talk component subtracted (dotted line). The strong central peak in the 3.5-cm spectrum is the enhanced echo from the south polar ice cap. Note the comparative weakness of the corresponding 12.6-cm feature.

clusion primarily on a comparison of the Arecibo CW and CLP data with Goldstone CW data from 1988 and 1990. The Goldstone monostatic CW data were particularly suitable for this comparison because of their simple and reliable calibration and because they covered the same 1988 and 1990 epochs as the Arecibo CW and CLP data, which eliminates any biases due to incidence angle or seasonal effects. For more details on the 1988–1990 Goldstone CW data set and a preliminary discussion of the south polar CW echo, see *Harmon et al.* [1992a].

5.1.1. Goldstone CW data. The 3.5-cm polar anomaly shows up as a narrow spike in the middle of the Doppler spectrum of the Goldstone SC echo. An example of a Goldstone 3.5-cm spectrum showing this feature is provided in Figure 13. (Here, as in the work by *Harmon et al.* [1992a], we plot our spectra in units of $\sigma_f f_o$, the normalized radar cross section per unit frequency times the center-to-limb Doppler bandwidth of Mars, in order to permit direct comparison of spectra taken at different times and/or different wavelengths.) The small offset of this feature from zero Doppler corresponds to the small polar offset of the residual ice cap (see the Doppler tracking plot of *Harmon et al.* [1992a, Figure 9]). A large number of these 3.5-cm spectra were obtained at various sub-Earth longitudes in 1988. In Figure 14a we show an average Doppler spectrum for the 3.5-cm polar feature; this was formed by shifting all of the 1988 Goldstone spectra by the mean Doppler shift of the residual ice cap, averaging, and then subtracting the broad nonpolar part of the spectrum. In Figure 14b we show the corresponding spectrum from averaging of 1990 Goldstone data. Overplotted on both these spectra are model spectra showing what one would expect if the enhanced backscatter is confined to and uniform over the residual ice cap. The good agreement shows that most of the scattering is confined to the residual ice cap, although there is some extra power in the wings due either to echo from outside the residual cap or to a small error in the assumed centroid of the ice cap. The model curve for the 1988 spectrum corresponds to an SC radar albedo (cross section per unit projected area) for the feature of 0.44 at a mean incidence angle of 65°, which is in reasonable agreement with the albedo estimated from VLA radar images at the same incidence angle and wavelength [*Butler*, 1994].

Figure 14 shows the polar feature to be considerably weaker in 1990 as compared to 1988, an effect which can

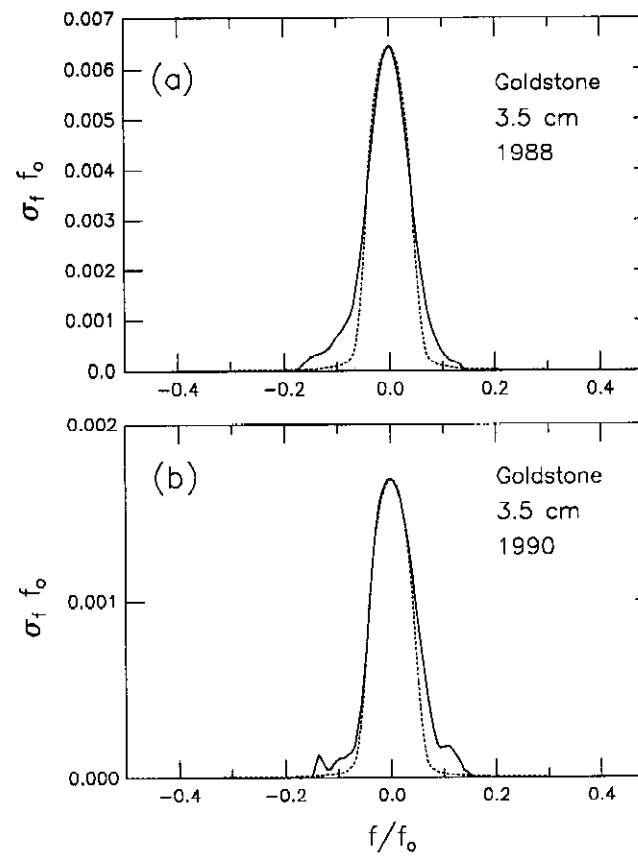

Figure 14. Doppler spectra of the 3.5-cm south polar feature from Goldstone CW spectra obtained during the (a) 1988 and (b) 1990 Mars oppositions. The 1988 spectrum is averaged over 59 observing runs with sub-Earth latitudes between 24.5°S and 25.5°S; the 1990 spectrum is averaged over 45 runs with sub-Earth latitudes between 10.8°S and 13.2°S. The spectrum of each run has been shifted by the mean Doppler offset of the residual ice cap before averaging. The mean incidence angle of the south polar ice cap is 65.2° in Figure 14a and 77.3° in Figure 14b. Also shown are model spectra (dotted lines) showing the ice cap echo corresponding to equivalent full-disk SC cross sections of 0.65 (Figure 14a) and 0.54 (Figure 14b) for the case of an assumed n=1.7 cosine scattering law.

be attribute to the higher incidence angles. Integrating under the spectra in Figure 14 gives cross sections of 0.672×10^{-3} at a mean incidence angle angle of 65.2° for 1988 and 0.211×10^{-3} at a mean incidence angle of 77.4° for 1990. If we assume a $\sigma^o_{sc}(\theta) \propto \cos^n \theta$ scattering law for the polar echo, which is reasonable, given the Galilean satellite results [*Ostro et al.*, 1992], then the 1988/1990 difference gives n=1.77. This is consistent with the n=1.3–1.8 values that have been found for the Galilean satellite echoes [*Ostro et al.*, 1992]. If one measures σ^o_{sc} at a reference incidence angle θ, then the corresponding equivalent full-disk albedo is $\hat{\sigma}^{eq}_{sc} = 2\sigma^o_{sc}(\theta)/[(n+1)\cos^n \theta]$. Using this and the model fits in Figure 14, we estimate $\hat{\sigma}^{eq}_{sc} \approx 0.6$ for the 3.5-cm south polar anomaly. For comparison, the depolarized albedos of the icy Galilean satellites range from 0.4 (Callisto) to 1.4 (Europa) and the mean $\hat{\sigma}^{eq}_{sc}$ for the permanently shaded portions of Mercury's polar craters is 0.59 [*Harmon*, 1997a].

5.1.2. Comparison with Arecibo data. Plotted with the 3.5-cm spectrum in Figure 13 is a 12.6-cm Arecibo spectrum obtained at about the same sub-Earth position and epoch. Unlike the 3.5-cm spectrum, the 12.6-cm spectrum peaks at zero Doppler. This is due to polarization crosstalk in the Arecibo antenna, which couples a fraction (of order 1%) of the OC echo into the SC component. To estimate the true polar cap contribution, we have multiplied the OC spectrum by 0.006 (0.6% crosstalk) and subtracted that from the SC spectrum, giving the dashed curve in Figure 13. Despite some uncertainty in the precise crosstalk factor, there is no way to avoid the conclusion that the 12.6-cm feature from the south polar ice cap is much weaker than its 3.5-cm counterpart. Comparison of Arecibo CLP and Goldstone CW data from 1990 provides further evidence of this strong wavelength dependence. In Figure 15a we show a spectrum from December 15, 1990, which was formed by summing the CLP delay-Doppler array over the delay bins containing the residual ice cap; also shown for comparison is the spectrum for a similar block of delay bins just in front of the ice cap (Figure 15b). Note that the spectrum from the delays containing ice cap shows a weak central feature, which we attribute to enhanced polar cap backscatter. This feature is free of confusion from polarization crosstalk since delay discrimination has isolated the polar delays from the strong quasi-specular glare at the front of the planet. For comparison, we show the average polar feature spectrum from the 1990 Goldstone CW data, adjusted for the slightly different incidence angle (Figure 15a). This shows the 12.6-cm feature to be about a factor of 3 weaker than the 3.5-cm feature.

5.1.3. Discussion: wavelength dependence. There are two basic ways to induce a wavelength dependence of the form observed. The first is to concentrate the size distribution of the subsurface irregularities at scales that preferentially scatter the shorter wavelength or to have a broad size distribution that cuts off at the larger scales (so that the scattering is pseudo-Rayleigh at S-band but not at X-band). The second way to effect a wavelength dependence is to reduce the depth of the scattering layer to the point where it is no longer capable of significant radar attenuation at the longer wavelength (i.e., becomes optically thin) [*Burns*, 1969, 1970]. Limiting the depth of the scattering layer can be effected in several ways, as is illustrated in the cartoons in Figure 16. One possibility is that the ice cap's properties change with depth; in this case one could limit the scattering at the longer wavelength by concentrating the scatterers at shallow depths (Figure 16a) or by having the ice become increasingly lossy with depth (Figure 16b). The alternative and, in some respects, simpler possibility is that the ice cap's structural and dielectric properties are independent of depth (Figure

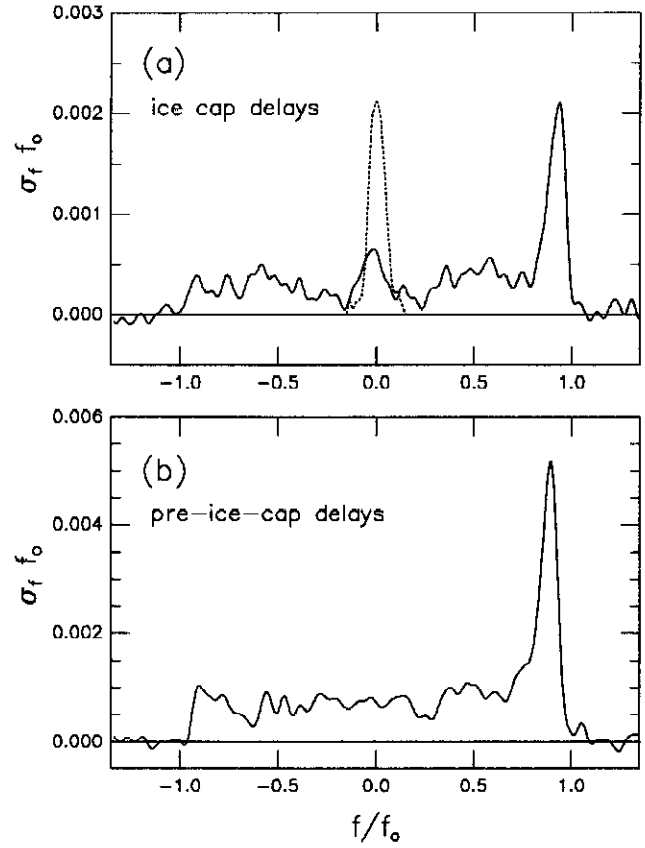

Figure 15. Doppler spectra formed by summing Arecibo CLP data over blocks of (a) 30 delay bins that include the residual south polar ice cap and (b) 30 delay bins immediately in front of the ice cap. The data were averaged over six observing runs from December 15, 1990. The spectra were smoothed over 10 frequency bins. The mean sub-Earth point is 42°W, 12.2°S. The small central peak in Figure 15a is the 12.6-cm enhancement feature from the south polar ice cap. Overplotted on this (dotted line) is the 3.5-cm south polar feature from Figure 14b, adjusted to the same mean incidence angle. The strong peak on the right limb is enhanced scattering from Tharsis/Olympus, amplified by a geometric effect in the delay-Doppler grid.

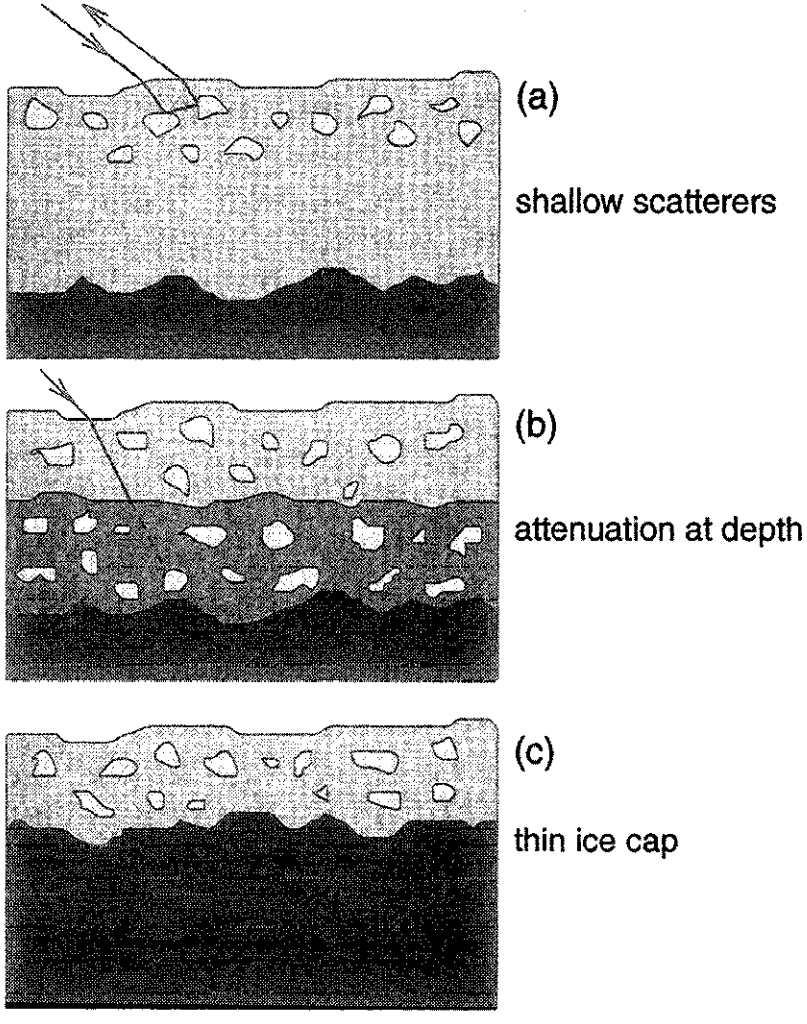

Figure 16. Cartoon showing possible subsurface scattering scenarios that might give the observed wavelength dependence for the south polar echo: (a) model with scatterers concentrated near the surface, (b) model with uniformly distributed scatterers but with stronger attenuation ("dirtier ice") at the greater depths, and (c) model with an ice cap that is thin relative to the radar attenuation depth. Black shading corresponds to bedrock; lighter shading corresponds to ice.

16c); in this case the optical-depth limitation corresponds to the case where the longer-wavelength wave passes largely unscattered and effectively undamped all the way through the ice cap to bedrock.

If one assumes that the "thin ice cap" model (Figure 16c) is the correct one, then one can use it to place an upper bound on the ice thickness by exploiting the requirement that the ice cap be thinner than the attenuation depth at the longer wavelength. The maximum attenuation depth will be for the case of pure ice with no contamination by dust particles. At an estimated temperature for the south polar cap of 142°K [*Paige and Ingersoll*, 1985], a 12.6-cm wave is attenuated at the rate of 1.5×10^{-5} neper/cm [*Warren*, 1984; *Thompson and Squyres*, 1990]. This corresponds to a $1/e$ two-way penetration depth of about 300 m. This also serves as the upper limit for the depth of the scattering layer in the "shallow scatterers" model (Figure 16a). One possible physical mechanism for the shallow scatterers model is preferential removal of the deeper scatterers by strong annealing of the ice, a mechanism mentioned by *Ostro and Shoemaker* [1990] as a reason why one might expect to see a weaker backscatter enhancement from the Galilean satellites at 70-cm wavelength. Data indicating a sharp drop in the Galilean satellite radar albedos between 12.6- and 70-cm wavelength have, in fact, been reported recently by *Black et al.* [1997] (who attribute the effect to the steepness of the scatterer size distribution rather than a finite depth for the scattering layer). It is interesting to note, however, that the Galilean satellites, unlike Mars' southern ice cap, show no wavelength dependence between 3.5 and 12.6 cm [*Ostro et al.*, 1992].

5.2. North Polar Cap

The 1992–1993 opposition offered the first opportunity to search for a north polar feature since the 1988

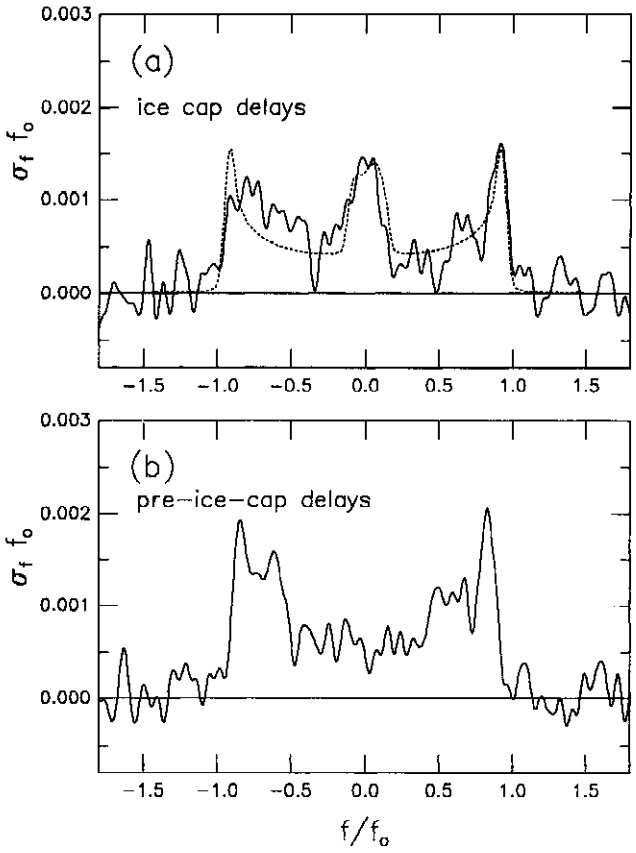

Figure 17. Doppler spectra (solid lines) formed by summing Arecibo CLP data over blocks of (a) 65 delay bins between the front of the north polar ice cap and the north pole and (b) 50 delay bins immediately in front of the ice cap. The data are an average of four runs from December 7, 1992. The spectra are smoothed over 14 frequency bins. The mean sub-Earth point is 323°W, 12.2°N. The central peak in Figure 17a is the 12.6-cm enhancement from the north polar ice cap. Also shown is a model spectrum (dotted line) for the case where $\hat{\sigma}_{sc}^{eq} = 0.12$ for the north polar icecap and $\hat{\sigma}_{sc}^{eq} = 0.016$ for the rest of the planet. The peaks at both limbs are caused by a geometric effect in the delay-Doppler grid.

discovery of Mars' south polar anomaly. Although the sub-Earth latitudes were not as favorable as in 1988, it was thought that the larger size and lower latitude limit of the northern ice cap would compensate for the relatively poor observing geometry. Our plan was to make observations on several days in early December 1992, when the sub-Earth latitude was at its highest and when the sub-Earth longitude was such that the offset side of the ice cap was most visible from Earth. Because of transmitter problems we were able to make observations on just one day (December 7) during this period, and on this date we did make a convincing detection of a north polar feature.

The north polar detection from December 7, 1992, is shown in Figure 17. The CLP delay-Doppler arrays from four consecutive observing runs were summed to increase signal/noise. The mean sub-Earth longitude for these runs was 322°W, and the latitude was 12.1°N. Figure 17a shows the SC Doppler spectrum formed by summing over all of the delay bins between the front of the ice cap (as seen from Earth) and the pole. Figure 17b shows the sum over the same number of delay bins in front of the ice cap. The spectrum in Figure 17a shows a central peak corresponding to enhanced backscatter from the north polar ice cap. The lack of a similar feature at the non-ice-cap delays (Figure 17b) gives added confidence that this is a real polar feature. Figure 17a shows a model spectrum overplotted on the data; this model assumes that the SC echo from the north polar ice cap has an equivalent full-disk albedo $\hat{\sigma}_{sc}^{eq}$ of 0.12 (assuming a $\cos^{1.8}\theta$ scattering law), whereas the rest of the planet has a $\hat{\sigma}_{sc}^{eq}$ of 0.016 (which is typical of the cratered highlands that dominate these longitudes). From this model we conclude that the 12.6-cm north polar feature is comparable in strength to the 12.6-cm south polar feature and much weaker than the 3.5-cm south polar feature.

Butler [1994] found no hint of a 3.5-cm north polar feature in Goldstone/VLA images from December 29, 1992, and January 12, 1993. Although the sub-Earth aspect of the ice cap was not favorably situated at those times, it is very difficult to avoid the conclusion that the north polar cap is intrinsically much less reflective than the south polar cap at 3.5-cm wavelength. There is even a possibility that the north polar echo is stronger at 12.6 cm than at 3.5 cm, i.e., that the wavelength dependence is the reverse of that seen for the south polar feature.

6. Conclusions

The new radar images confirm earlier indications that most of Mars' radar-bright features are associated with relatively young volcanic constructs and flows. However, the distribution of these bright features is found to be more complex than one might have predicted on the basis of the current standard geologic maps of the planet. Although some of the strongest echoes come from the major shield volcanoes, the echo distribution across a given shield tends to be very irregular. Some of the more prominent radar features are associated with relatively young off-shield flows such as the Olympus and Pavonis lava aprons. Also, most of the major volcanoes have radar-dark areas on their shields or in their immediate environs; these areas are probably associated with either ash eruptions or debris flows. All of these findings point toward an extreme heterogeneity in the decimeter-scale surface texture over the major volcanic provinces, which is consistent with complex volcanic histories.

One of our more intriguing findings is the extremely high absolute brightness seen on the Martian volcanoes and off-shield flows, with some features giving twice the σ_{sc}^{o} of some of the roughest lava flows on Earth. The implication is that the young Martian flows tend to be rougher or more intrinsically reflective than their terrestrial counterparts or have been modified by dust deposition and mass wasting to provide a layer which is more

conducive to volume scattering. Follow-up work on this problem with future radar observations and spacecraft landers should be a goal of future Mars studies.

The discovery of a depolarized feature from the north polar ice cap provides yet more evidence that enhanced backscatter is a common property of planetary ices. However, our 12.6-cm data show north and south polar features that are surprisingly weak in comparison with the strong 3.5-cm echoes detected from the south polar ice cap by *Muhleman et al.* [1991]. Since the enhanced backscatter is undoubtedly a volume scattering phenomenon, a plausible explanation is that the south polar cap simply becomes optically thin at the longer wavelength. Further observations will be needed to determine the wavelength dependence of the north polar enhancement.

Acknowledgments. The National Astronomy and Ionosphere Center (Arecibo Observatory) is operated by Cornell University under a cooperative agreement with the National Science Foundation and with support from the National Aeronautics and Space Administration (NASA). R.E.A. and E.A.G. were supported by grant NAGW-1358 to Washington University from the NASA Planetary Geology and Geophysics (PGG) Program Office. B.A.C. was supported by NASA PGG grant NAGW-3360. M.A.S. acknowledges support from the Jet Propulsion Laboratory, California Institute of Technology, under contract with NASA.

References

Arvidson, R., M. Shepard, E. Guinness, S. Petroy, J. Plaut, D. Evans, T. Farr, R. Greeley, N. Lancaster, and L. Gaddis, Characterization of lava flow degradation in the Pisgah and Cima volcanic fields, California, using Landsat Thematic Mapper and AIRSAR data, *Geol. Soc. Am. Bull., 105*, 175–188, 1993.

Black, G. J., D. B. Campbell, and P. D. Nicholson, Modeling the radar scattering properties of the icy Galilean satellites, paper presented at Workshop on Remote Sensing of Planetary Ices, U.S. Geol. Surv., Flagstaff, Arizona, 1997.

Burns, A. A., Diffuse component of lunar radar echoes, *J. Geophys. Res., 74*, 6553–6566, 1969.

Burns, A. A., On the wavelength dependence of radar echoes from the moon, *J. Geophys. Res., 75*, 1467–1482, 1970.

Butler, B. J., 3.5-cm radar investigation of Mars and Mercury: Planetological implications, Ph.D. thesis, Calif. Inst. of Technol., Pasadena, 1994.

Butler, B. J., D. O. Muhleman, and M. A. Slade, Mercury: Full-disk radar images and the detection and stability of ice at the north pole, *J. Geophys. Res, 98*, 15,003–15,023, 1993.

Campbell, B. A., R. E. Arvidson, and M. K. Shepard, Radar polarization properties of volcanic and playa surfaces: Applications to terrestrial remote sensing and Venus data interpretation, *J. Geophys. Res., 98*, 17,099–17,113, 1993.

Campbell, D. B., and B. A. Burns, Earth-based radar imagery of Venus, *J. Geophys. Res., 85*, 8271–8281, 1980.

Downs, G. S., P. E. Reichley, and R. R. Green, Radar measurements of Martian topography and surface properties: The 1971 and 1973 oppositions, *Icarus, 26*, 273–312, 1975.

Downs, G. S., P. J. Mouginis-Mark, S. H. Zisk, and T. W. Thompson, New radar-derived topography for the northern hemisphere of Mars, *J. Geophys. Res., 87*, 9747–9754, 1982.

Dyce, R. B., G. H. Pettengill, and A. D. Sanchez, Radar observations of Mars and Jupiter at 70 cm, *Astron. J., 71*, 771–777, 1967.

Edgett, K. S., B. J. Butler, J. R. Zimbelman, and V. E. Hamilton, Volatiles and volcanoes: Very late Amazonian ash deposits and explosive activity along the western flanks of the Tharsis Montes, Mars, paper presented at Workshop on Evolution of Martian Volatiles, Lunar Planet. Inst., Houston, Tex., Feb 12–14, 1996.

Edgett, K. S., B. J. Butler, J. R. Zimbelman, and V. E. Hamilton, Geologic context of the Mars radar "Stealth" region in southwestern Tharsis, *J. Geophys. Res., 102*, 21,545–21,567, 1997.

Goldstein, R. M., Mars: Radar observations, *Science, 150*, 1715–1717, 1965.

Golombek, M. P., R. A. Cook, H. J. Moore, and T. J. Parker, Selection of the Mars Pathfinder landing site, *J. Geophys. Res., 102*, 3967–3988, 1997.

Greeley, R., and J. E. Guest, Geologic map of the eastern equatorial region of Mars, 1:15,000,000 *Geol. Ser. Map I-1802-B*, U.S. Geol. Surv., Reston, Va., 1987.

Hagfors, T., and W. Kofman, Mapping of overspread targets in radar astronomy, *Radio Sci., 26*, 403–416, 1991.

Hanley, D., and J. R. Zimbelman, Topographic control of lava flow emplacement: Earth, Mars, and Venus, paper presented at the 26th Lunar and Planetary Science Conference, Houston, Tex., 1995.

Hapke, B., Coherent backscatter and the radar characteristics of outer planet satellites, *Icarus, 88*, 407–417, 1990.

Harmon, J. K., Mercury radar studies and lunar comparisons, *Adv. Space Res., 19* (10), 1487–1496, 1997a.

Harmon, J. K., A radar study of the Chryse region, Mars, *J. Geophys. Res., 102*, 4081–4095, 1997b.

Harmon, J. K., and S. J. Ostro, Mars: Dual-polarization radar observations with extended coverage, *Icarus, 62*, 110–128, 1985.

Harmon, J. K., and M. A. Slade, Radar mapping of Mercury: Full-disk images and polar anomalies, *Science, 258*, 640–643, 1992.

Harmon, J. K., D. B. Campbell, and S. J. Ostro, Dual-polarization radar observations of Mars: Tharsis and environs, *Icarus, 52*, 171–187, 1982.

Harmon, J. K., M. A. Slade, and R. S. Hudson, Mars radar scattering: Arecibo/Goldstone results at 12.6- and 3.5-cm wavelengths, *Icarus, 98*, 240–253, 1992a.

Harmon, J. K., M. P. Sulzer, P. J. Perillat, and J. F. Chandler, Mars radar mapping: Strong backscatter from the Elysium basin and outflow channel, *Icarus, 95*, 153–156, 1992b.

Harmon, J. K., S. J. Ostro, J. F. Chandler, and R. S. Hudson, Radar ranging to Ganymede and Callisto, *Astron. J., 107*, 1175–1181, 1994a.

Harmon, J. K., M. A. Slade, R. A. Velez, A. Crespo, M. J. Dryer, and J. M. Johnson, Radar mapping of Mercury's polar anomalies, *Nature, 369*, 213–215, 1994b.

Hodges, C. A., and H. J. Moore, *Atlas of Volcanic Landforms on Mars*, U.S. Geol. Surv., Washington, D.C., 1994.

Jakosky, B. M., and D. O. Muhleman, A comparison of the thermal and radar characteristics of Mars, *Icarus, 45*, 25–38, 1981.

Moore, H. J., and T. W. Thompson, A radar-echo model for Mars, *Proc. Lunar and Planet. Sci. Conf., 21st*, 457–472, 1991.

Mouginis-Mark, P. J., S. H. Zisk, and G. S. Downs, Ancient and modern slopes in the Tharsis region of Mars, *Nature, 297*, 546–550, 1982.

Mouginis-Mark, P. J., L. Wilson, J. W. Head, S. H. Brown, J. L. Hall, and K. D. Sullivan, Elysium Planitia: Regional

geology, volcanology and evidence for volcano-ground ice interactions, *Earth Moon Planets, 30*, 149–173, 1984.

Muhleman, D. O., B. J. Butler, A. W. Grossman, and M. A. Slade, Radar images of Mars, *Science, 253*, 1508–1513, 1991.

Muhleman, D. O., A. W. Grossman, and B. J. Butler, Radar investigation of Mars, Mercury, and Titan, *Annu. Rev. Earth Planet. Sci., 23*, 337-374, 1995.

Ostro, S. J., and E. M. Shoemaker, The extraordinary radar echoes from Europa, Ganymede, and Callisto: A geological perspective, *Icarus, 85*, 335–345, 1990.

Ostro, S. J., et al., Europa, Ganymede, and Callisto: New radar results from Arecibo and Goldstone, *J. Geophys. Res., 97*, 18,227–18,244, 1992.

Paige, D. A., and A. P. Ingersoll, Annual heat balance of Martian polar caps: Viking observations, *Science, 228*, 1160–1168, 1985.

Plescia, J. B., Recent flood lavas in the Elysium region of Mars, *Icarus, 88*, 465–490, 1990.

Schaber, G. G., Radar, visual and thermal characteristics of Mars: Rough planar surfaces, *Icarus, 42*, 159–184, 1980.

Schultz, P. H., and A. B. Lutz, Polar wandering of Mars, *Icarus, 73*, 91–141, 1988.

Scott, D. H., and M. G. Chapman, Mars Elysium Basin: Geologic/volumetric analyses of a young lake and exobiologic implications, *Proc. Lunar Planet. Sci. Conf., 21st*, 669–677, 1991.

Scott, D. H., and K. L. Tanaka, Ignimbrites of Amazonis Planitia region of Mars, *J. Geophys. Res., 87*, 1179–1190, 1982.

Scott, D. H., and K. L. Tanaka, Geologic map of the western equatorial region of Mars, 1:15,000,000, *Geol. Ser. Map I-1802-A*, U.S. Geol. Surv., Reston, Va.,1986.

Simpson, R. A., G. L. Tyler, and D. B. Campbell, Arecibo radar observations of Mars surface characteristics near the equator, *Icarus, 33*, 102–115, 1978a.

Simpson, R. A., G. L. Tyler, and D. B. Campbell, Arecibo radar observations of Mars surface characteristics in the northern hemisphere, *Icarus, 36*, 153–173, 1978b.

Simpson, R. A., J. K. Harmon, S. H. Zisk, T. W. Thompson, and D. O. Muhleman, Radar determination of Mars surface properties, in *Mars*, edited by H. Kieffer et al., pp. 652–685, Univ. of Arizona Press, Tucson, 1992.

Slade, M. A., B. J. Butler, and D. O. Muhleman, Mercury radar imaging: Evidence for polar ice, *Science, 258*, 635–640, 1992.

Sulzer, M. P., A radar technique for high range resolution incoherent scatter autocorrelation function measurements utilizing the full average power of klystron radars, *Radio Sci., 21*, 1033–1040, 1986.

Sulzer, M. P., Recent incoherent scatter techniques, *Adv. Space Res., 9* (5), 153–162, 1989.

Thompson, T. W., and H. J. Moore, A model for depolarized radar echoes from Mars, *Proc. Lunar Planet. Sci. Conf., 19th*, 409–422, 1989.

Thompson, W. R., and S. W. Squyres, Titan and other icy satellites: Dielectric properties of constituent materials and implications for radar sounding, *Icarus, 86*, 336–354, 1990.

Warren, S. J., Optical constants of ice from the ultraviolet to the microwave, *Appl. Opt., 23*, 1206–1225, 1984.

Wilson, L., and J. W. Head, Mars: Review and analysis of volcanic eruption theory and relationships to observed landforms, *Rev. Geophys., 32*, 221–263, 1994.

Zimbelman, J., A. Johnston, C. Lovett, and D. Jensen, Geologic map of the Ascraeus Mons volcano, Mars, paper presented at the 27th Lunar and Planetary Science Conference, Lunar Planet. Inst., Houston, Tex., 1996.

R. E. Arvidson and E. A. Guinness, Department of Earth and Planetary Sciences, Washington University, Campus Box 1169, One Brookings Drive, St. Louis, MO 63130. (arvidson@wunder.wustl.edu)

B. A. Campbell, National Air and Space Museum, MRC 315, Washington, DC 20560. (campbell@ceps.nasm.edu)

J. K. Harmon, Arecibo Observatory, National Astronomy and Ionosphere Center, HC3 Box 53995, Arecibo, PR 00612. (harmon@naic.edu)

M. A. Slade, Jet Propulsion Laboratory, MS 238-420, 4800 Oak Grove Drive, Pasadena, CA 91109. (marty@shannon.jpl.nasa.gov)

(Received June 12, 1998; revised November 27, 1998; accepted December 1, 1998.)